

New Interpretable Statistics for Large Scale Structure Analysis and Generation

E. Allys*

*Laboratoire de Physique de l'cole Normale Suprieure, ENS, Universit PSL,
CNRS, Sorbonne Universit, Universit de Paris, F-75005 Paris, France*

T. Marchand*

*DI, cole Normale Suprieure, ENS, Universit PSL, Paris, France
Laboratoire de Physique de l'cole Normale Suprieure,
ENS, Universit PSL, CNRS, Sorbonne Universit,
Universit de Paris, F-75005 Paris, France*

J.-F. Cardoso

CNRS and Sorbonne Universit, UMR 7095, Institut dAstrophysique de Paris, 98 bis Boulevard Arago, 75014 Paris, France

F. Villaescusa-Navarro

*Department of Astrophysical Sciences, Princeton University, Peyton Hall, Princeton NJ 08544, USA
Center for Computational Astrophysics, Flatiron Institute, 162 5th Avenue, New York NY 10010, USA*

S. Ho

*Center for Computational Astrophysics, Flatiron Institute, 162 5th Avenue, New York NY 10010, USA
Department of Astrophysical Sciences, Princeton University, Peyton Hall, Princeton NJ 08544, USA*

S. Mallat

*Collge de France, Paris, France
Center for Computational Mathematics, Flatiron Institute,
162 5th Avenue, New York NY 10010, USA
DI, cole Normale Suprieure, ENS,
Universit PSL, Paris, France
(Dated: June 15, 2022)*

This paper introduces the Wavelet Phase Harmonics (WPH) statistics. They are interpretable low-dimensional statistics which describe 2D non-Gaussian density fields. These statistics are built from WPH moments, which have been recently introduced in data science and machine learning community. In this paper, we applied WPH statistics to projected matter density fields from the Quijote N-body simulations. We find by computing the Fisher information matrix, that the WPH statistics can place more stringent constraints on 5 cosmological parameters when compared to the combination of power-spectrum and bi-spectrum. We also use the WPH statistics to successfully generate from a maximum entropy model new 2D density fields that reproduce the PDF, mean, power-spectrum, bispectrum and the Minkowski functionals of the input density fields. While separate methods have been proven very efficient for parameter estimations and statistical syntheses for large scale structure, WPH statistics are the first statistics that can both achieve a more stringent cosmological parameter constraint, and produce a sufficiently accurate simulation of the Universe while being interpretable.

I. INTRODUCTION

The evolution of the Large Scale Structure (LSS) of the Universe shows how non-linearities affect the statistical properties of a field. Starting from a Gaussian distribution in the early Universe, the fluctuations of the density field grew into a complex structure containing walls, filaments, nodes, and voids – the cosmic web. These structures are direct signatures of the coupling of the different scales in the cosmic web.

In contrast to Cosmic Microwave Background (CMB) observations, where most information on the cosmological model has been statistically extracted, no generic and efficient statistical characterization of the LSS exists. The primary temperature anisotropies of the CMB are very well characterized by a Gaussian field, therefore they can be described fully using their power spectrum. In other words, for a homogeneous and

isotropic Gaussian field, there is no interaction between the different scales, and such fields are entirely characterized by the amplitude of their Fourier modes. On the other hand, the LSS field is a non-Gaussian field with long-range interactions. There are couplings between different scales which are not described by the power-spectrum alone.

A standard method to capture the non-linearity of the LSS is to compute n^{th} -order point correlation functions, which correspond to poly-spectra when expressed in terms of Fourier modes. In particular, the bispectrum (poly-spectrum for $n = 3$) has been widely used in the last decades to study the LSS [see for instance 1–3]. One difficulty of directly using the Fourier bispectrum is its important number of terms, which generally leads to the construction of tailored bispectrum estimators [see for instance 4]. In addition, bispectrum estimators, as any high order moments, are very sensitive to outliers and thus may suffer high empirical variance [5].

Alternatively, other statistics have been developed to go beyond bispectrum analysis of the LSS fields. For example, the line correlation function (LCF) has been applied to the

* Both authors contributed equally to this work.

LSS, to characterize it and to perform cosmological parameter inference [6–8]. Such descriptors, that compute pure phase information in Fourier space, are particularly efficient to describe filamentary structures such as the LSS, especially in addition to power spectrum and bispectrum [2, 9]. One could also cite an abundant literature on other statistics, such as those related to the distribution of peaks [10] or of voids [11] in the cosmic web.

A characteristic of non-Gaussian fields such as the LSS is that they contain coherent structures at different scales that are well localized in space and in frequency. This motivates a hierarchical multiscale approach, such as the wavelet transform, rather than a description in terms of Fourier modes which are not localized in space. The wavelet transform, which has been applied to various physical fields, decomposes a process at different scales and locations. Moreover, it often yields a sparse spatial description [12–16].

While being an adequate tool to perform an efficient sparse multiscale description of non-Gaussian fields, the wavelet transform in itself does not characterize interactions between scales. Indeed, second order moments of a wavelet transform depend solely on the power-spectrum [15, 17, 18]. We can however capture interaction between scales by computing the correlations between non-linear transforms of the wavelet coefficients. In this way, one obtains statistical descriptors characterizing the dependence across different scales that are signatures of the coherent structures of the field.

Recently, [19] introduced a novel low-dimensional statistical description following these principles. They applied a non-linear operator, called the *phase harmonic operator*, on the multi-scale wavelet transform of a field. This operator acts on the complex phase of a field and enables to align the phase information across different scales. The statistical description it leads to is called *Wavelet Phase Harmonics* (WPH) statistics. These statistics are constructed from WPH moments, *i.e.*, covariances of wavelet transforms whose spatial frequencies have been made synchronous by means of the phase harmonic operator. WPH statistics are able to capture the coupling between scales and are efficient in reproducing various textures [20], as well as obtaining competitive classification results on data sets as challenging as ImageNet [21].

Building upon these recent results, we design in this paper low-dimensional WPH statistics suited for the matter density field of the LSS. One strength of this work is the method used to construct and validate these statistics, which relies on performing simultaneously two complementary tasks: i) measuring cosmological information and ii) statistical syntheses. For the former, we compute the Fisher information with respect to five cosmological parameters contained in these statistics. For the latter, we generate syntheses of the LSS matter density field by building a maximum entropy generative model. Such a model generates new realizations that are conditioned on the WPH statistics, but are otherwise *as general as possible* (*i.e.*, they do not include any additional implicit or explicit constraint). The quality of the syntheses is assessed by checking whether they reproduce standard cosmological statistics such as the power spectrum, bispectra, and Minkowski functionals. For both these tasks, we obtain state-of-the-art result, which is the main

result of this paper. While previous approaches are successful in each of these tasks, it is, up to our knowledge, the first time that state-of-the-art results are obtained for both these tasks from the same low-dimensional statistical description.

Additionally, we discuss which kind of information is described by the different WPH moments, exhibiting the interpretability of WPH statistics. It allows us to physically comprehend the different results obtained for the LSS matter density field. In this paper, we illustrate in particular which part of the foamy structure of the LSS is related to the interaction between close and distant scales. We also exhibit how the information about the different cosmological parameter is distributed in the coupling between different scales.

Outline of the paper. We base our work on two-dimensional projected matter density fields from the Quijote N-body simulations of the LSS [22]. We present in Sec. II the general form of the low dimensional WPH statistical description that is used in the whole paper. A brief description of the Quijote simulation, as well as the Fisher analysis results on cosmological parameters are given in Sec. III. In Sec. IV, we present the microcanonical maximum entropy generative model that we use, and we validate the statistical properties of the syntheses obtained from WPH statistical constraints. The complete parameters of the WPH representations used to perform both cosmological Fisher analysis and statistical syntheses are given in App. A. Finally, we discuss in Sec. V the physical interpretation of the WPH coefficients, as well as their link with standard summary statistics.

Notations. The random 2d field under study is denoted $\rho(\vec{x})$. In all the paper, we assume that this field $\rho(\vec{x})$ has homogeneous statistical properties, *i.e.*, that the statistical distribution of the associated process is translation invariant. We also assume that this field has boundary periodic conditions. As we work on a Cartesian grid, the position \vec{x} is defined in $[0, N]^2$, where N refers to the size of the grid ($N = 256$ in the whole paper). The Fourier transform of $A(\vec{x})$ is $\hat{A}(\vec{k})$. The symbol $*$ stands for a convolution, and A^* is the complex conjugate of A . If X and Y are two stochastic processes, we note $\langle X \rangle$ the expected value of X , and $\text{Cov}(X, Y)$ the covariance between X and Y which is defined as $\text{Cov}(X, Y) = \langle XY^* \rangle - \langle X \rangle \langle Y^* \rangle$.

A public version of the code used in this article is available at https://github.com/Ttantto/wph_quijote.

II. WAVELET PHASE HARMONICS

A. Wavelet transform

WPH statistics are based on the wavelet transform. This transform, that has been widely used in physical applications [see for instance 14], is very efficient to locally separate the multiscale variability of a given process. A wavelet transform is built from the convolution of a field under study by a set of wavelets that each probe specific structures. When appropriate wavelets are chosen, the wavelet transform also yields a sparse spatial description of the structures at different scales. The wavelets used in this paper are bump steerable wavelets, which characterize localized directional oscillations.

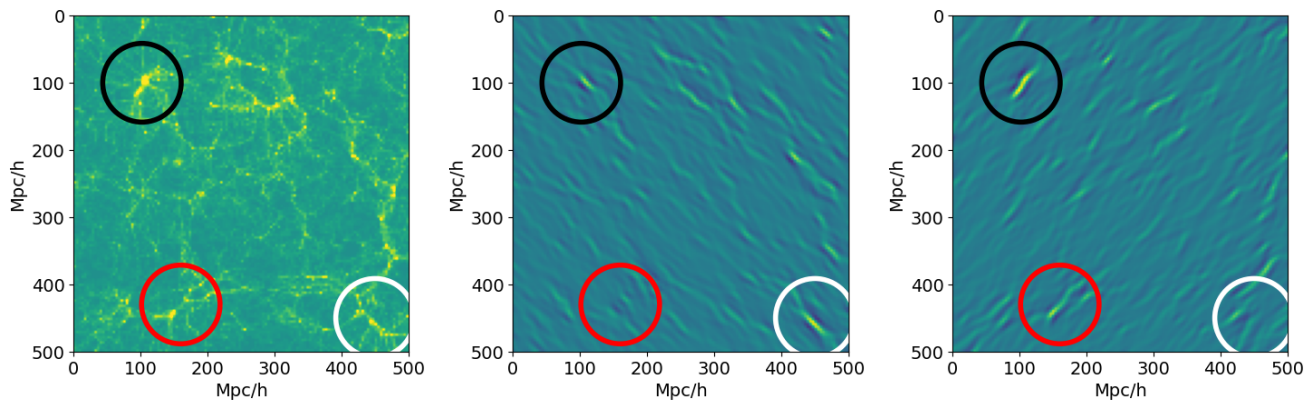


FIG. 1: (Left) Typical projected 2D density maps of the LSS from the Quijote simulation. (Center and Right) Real-part of the same maps convolved by wavelets with $j = 1$ and $\ell = +2$ and $\ell = -2$, respectively. The red circles highlight filaments that are captured by the first wavelet, the white circle a filament that is captured by the second wavelet and the black circle highlights an intersection of filaments captured by both wavelets.

These wavelets, introduced in [19], have been shown efficient to synthesize physical fields [20].

The complex bump steerable wavelets $\psi_{j,\ell}(\vec{x})$ are labeled by two integers j and ℓ . The integer j takes J values between 0 and $J - 1$ and specifies the characteristic scale of oscillation, which is of order 2^j in pixel space. The integer ℓ characterizes their orientation. In this paper, we divide 2π in $L = 16$ angles. Therefore, an angle indexed by ℓ corresponds to $2\pi\ell/L$ radian with respect to the reference axis. All these wavelets are obtained by dilatation and rotation of the same complex mother wavelet $\psi(\vec{x})$:

$$\psi_{j,\ell}(\vec{x}) = 2^{-j}\psi(2^{-j}r_{-\ell}\vec{x}), \quad (1)$$

where r_{ℓ} is the rotation of angle $2\pi\ell/L$. The definition of the mother bump-steerable wavelet is given in App. B 1. The real part of such a wavelet, as well as its Fourier transform (which is real) are given in Fig. 2.

The Fourier transform of each wavelet $\hat{\psi}_{j,\ell}(\vec{k})$ samples a limited region of the Fourier plane. In the following, we index the wavelets by their central frequency $\vec{\xi}$, which yields for a given pair (j, ℓ) :

$$\vec{\xi} = 2^{-j}r_{\ell}\vec{\xi}_0, \quad (2)$$

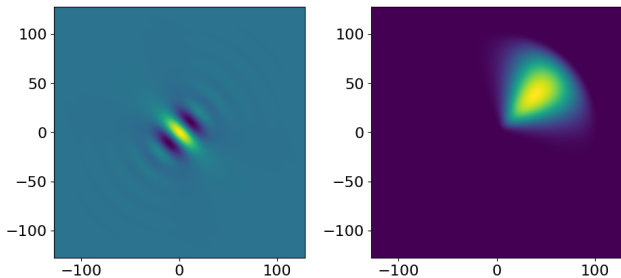


FIG. 2: Two-dimensional bump-steerable wavelets (see Appendix B 1). (Left): Real part of $\psi_{j,\ell}$ for $j = 4$ and $\ell = 2$. (Right) Fourier transform of $\psi_{j,\ell}$ for $j = 1$ $\ell = 2$. Note that this Fourier transform is real.

where $\vec{\xi}_0$ is the central frequency of the mother wavelet ψ . This means that

$$\psi_{\vec{\xi}}(\vec{x}) = \psi_{j,\ell}(\vec{x}), \quad (3)$$

for (j, ℓ) that verify Eq. (2). When the integers j span all the possible values for a given image (*i.e.*, when 2^j is the size of the image), the $\hat{\psi}_{\vec{\xi}}(\vec{k})$ wavelet spectral bands for all j and ℓ values covers the whole Fourier plane.

The bump-steerable wavelet transform of a field $\rho(\vec{x})$ is defined as its convolution with the set of wavelets defined above. This wavelet transform contains $J \times L$ convolutions $\rho * \psi_{\vec{\xi}}(\vec{x})$. Each of these convolutions corresponds to a local filtering of the field ρ on the frequency support of $\psi_{\vec{\xi}}$, around the $\vec{\xi}$ frequency. Examples of such convolutions on matter density fields of the LSS are given in Fig. 1. One sees in this figure how the filamentary structures at a given scale and orientation are efficiently picked up by the wavelets, that probe localized directional oscillations. This figure also displays the sparsity of the wavelet transform used, since the resulting filtered fields have large values only at few spatial positions.

B. Covariance of wavelet transforms

From the multiscale decomposition performed by the wavelet transform, one can build summary statistics that quantify the coupling between the different scales of a field. In order to characterize the dependency between the field filtered at two scales (*i.e.* $\rho * \psi_{\vec{\xi}_1}(\vec{x})$ and $\rho * \psi_{\vec{\xi}_2}(\vec{x})$), one can consider the covariance:

$$C_{\vec{\xi}_1, \vec{\xi}_2}(\vec{\tau}) = \text{Cov} \left[\rho * \psi_{\vec{\xi}_1}(\vec{x}), \rho * \psi_{\vec{\xi}_2}(\vec{x} + \vec{\tau}) \right]. \quad (4)$$

which does not depend on \vec{x} for a stationary field but only on the spatial shift $\vec{\tau}$. However, such quantities do not carry more

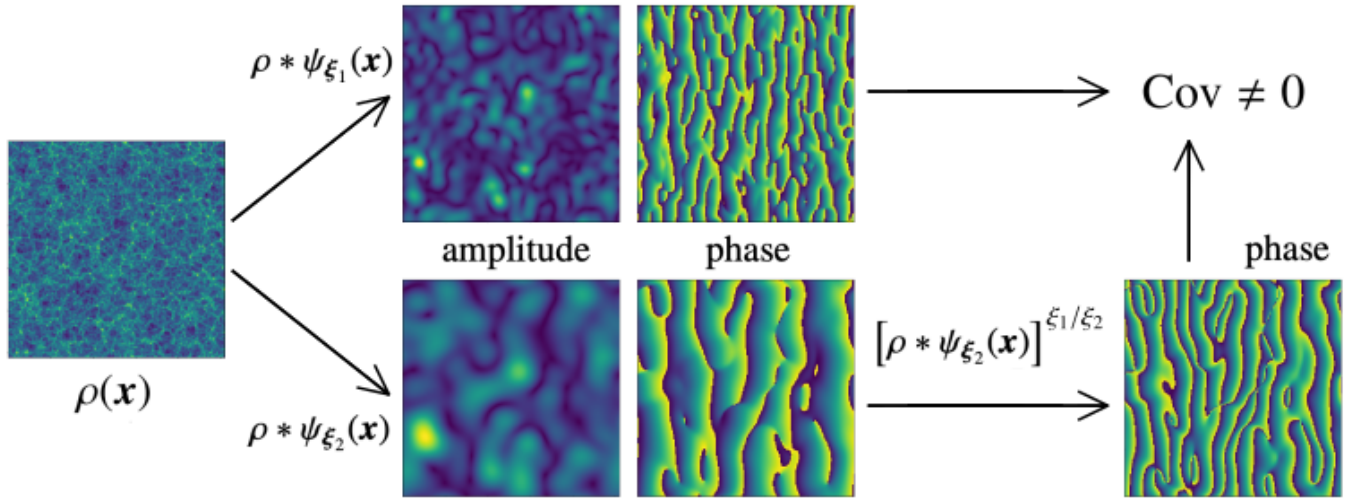


FIG. 3: Illustration of WPH moments computation. A convolution of a Quijote density field ρ by two wavelets ψ_{ξ_1} and ψ_{ξ_2} is shown, with $(j_1, \ell_1) = (3, 0)$ and $(j_2, \ell_2) = (4, 0)$. The amplitude and phase of each convolution is shown in the central panel. From their phase, one sees that both $\rho * \psi_{\xi_1}$ fields oscillate with different 2^{j_1} and 2^{j_2} characteristic wavelengths, respectively. Their covariance is therefore negligible. By applying the phase harmonic operator to $\rho * \psi_{\xi_2}$, selecting $p_2 = \xi_1/\xi_2$, one obtains a new field of same amplitude but with a phase of 2^{j_2} characteristic wavelength (right panel). As the fields $\rho * \psi_{\xi_1}$ and $[\rho * \psi_{\xi_2}]^{\xi_1/\xi_2}$ have the same characteristic wavelength, their covariance is *a priori* non-negligible. Such WPH moment characterizes the relative phase alignment between $\rho * \psi_{\xi_1}$ and $\rho * \psi_{\xi_2}$ fields. Note that this WPH moment computation is illustrated in Fourier space in the left panel of Fig. 11

information than the power spectrum $S(\vec{k})$ of ρ ¹ since they are related by [20]:

$$C_{\vec{\xi}_1, \vec{\xi}_2}(\vec{\tau}) = \int S(\vec{k}) \hat{\psi}_{\vec{\xi}_1}(\vec{k}) \hat{\psi}_{\vec{\xi}_2}^*(\vec{k}) e^{-i\vec{k} \cdot \vec{\tau}} d\vec{k}. \quad (5)$$

This relation also shows that, while the $C_{\vec{\xi}_1, \vec{\xi}_2}(\vec{\tau})$ coefficients involve various scales and angles, they do not actually capture the couplings between them. Indeed, it implies that $C_{\vec{\xi}_1, \vec{\xi}_2}(\vec{\tau}) = 0$ if the supports of $\psi_{\vec{\xi}_1}$ and $\psi_{\vec{\xi}_2}$ in the Fourier plane do not overlap. This is illustrated in Fig. 3, where two convolutions of a typical LSS field by wavelets probing different spatial frequencies $\vec{\xi}_1$ and $\vec{\xi}_2$ are shown. Since the covariance of those maps is basically their scalar product², it is negligible because the maps oscillate at different spatial frequencies. These results imply that the descriptor $C_{\vec{\xi}_1, \vec{\xi}_2}(\vec{\tau})$ cannot capture any coupling between different scales or angles. As a consequence, this descriptor cannot distinguish between processes that have the same power spectrum, but different higher order statistics, even when comparing a Gaussian process with a highly non-Gaussian one.

C. Phase harmonics and coupling between scales

The statistical dependence between non-overlapping scales must be captured using non-linear operators. To do so, we use the phase harmonic operator introduced in [19]: given a complex number $z \in \mathbb{C}$, with modulus $|z|$ and phase $\arg(z)$, its p^{th} phase harmonic is noted $[z]$ and is defined as

$$[z]^p = |z| \cdot e^{ip \arg(z)}. \quad (6)$$

When we apply this operator on a two-dimensional complex map, it ‘accelerates’ its spatial frequency of oscillation by a factor p , while keeping its modulus unchanged. This non-linear operation is illustrated in Fig. 3, where the phase harmonic applied to wavelet transforms $\rho * \psi_{\vec{\xi}_2}$ creates a non-vanishing covariance, hence capturing the local dependency between different scales of the field. Indeed, while this operator does not modify the spatial localization of the features of $\rho * \psi_{\vec{\xi}_2}$ fields, it modifies their Fourier spectrum. The spectral band of $\rho * \psi_{\vec{\xi}_2}$ is localized around frequency $\vec{\xi}_2$, while the $[\rho * \psi_{\vec{\xi}_2}]^p$ field mainly contains frequencies around $p\vec{\xi}_2$. Hence, we shall consider couplings between $\vec{\xi}_1$ and $\vec{\xi}_2$ frequencies, quantified by so-called *WPH moments* defined as

$$C_{\vec{\xi}_1, p_1 \vec{\xi}_2, p_2}(\vec{\tau}) = \text{Cov} \left([\rho * \psi_{\vec{\xi}_1}(\vec{x})]^{p_1}, [\rho * \psi_{\vec{\xi}_2}(\vec{x} + \vec{\tau})]^{p_2} \right). \quad (7)$$

In order to obtain non vanishing WPH moments, it is necessary that the frequency bands of $[\rho * \psi_{\vec{\xi}_1}(\vec{x})]^{p_1}$ and $[\rho * \psi_{\vec{\xi}_2}(\vec{x})]^{p_2}$ overlap significantly, which is guaranteed if

$$p_1 \vec{\xi}_1 \simeq p_2 \vec{\xi}_2, \quad (8)$$

¹ $S(\vec{k})$ is the complete power spectrum, and not the isotropic one. For a stationary process ρ , it is defined as the Fourier transform of the two-points correlation function $s(\vec{\tau}) = \text{Cov}[\rho(\vec{u}), \rho(\vec{u} + \vec{\tau})]$.

² Indeed, the mean values of the wavelet convolutions vanish, and the covariance of processes A and B of vanishing expectations verifies $\text{Cov}(A, B) = \langle AB^* \rangle$.

as illustrated in Fig. 3. Empirical estimates of the WPH moments are easily computed from samples of the field on an $N \times N$ grid.

A key property of phase harmonics is its *robustness*. While phase harmonics $[z]^p$ and standard moments z^p capture the same phase couplings, the former are estimated more robustly than the latter because their modulus is not raised to the p -th power as with standard moments³. As an example, coupling characteristic scales of 4 and 32 pixels would require raising the field to the 8-th power and would make standard moments extremely susceptible to outliers. It follows that the variance of the WPH moments is bounded more favorably than the variance of standard n -point statistics (see [20] for a theoretical analysis).

The *WPH statistics* introduced in this paper are built from a collection of WPH moments given in Eq. (7). Constructing a set of WPH statistics boils down to selecting an ensemble of WPH moments, which are defined by $(\vec{\xi}_1, p_1, \vec{\xi}_2, p_2)$ parameters. This selection is to be tailored depending on the purpose of the WPH statistics and on the field on which they are applied.

D. Symmetries and spatial shift discretization

Symmetries and invariant WPH description If the physical phenomenon under study possesses some symmetries (*i.e.*, if its statistical properties are invariant under certain groups of transformations), we can take them into account and lower the dimension of the WPH statistics. Note that translation invariance was considered from the outset.

If the field is invariant under rotations, the angular dependency of the WPH moments only depends on $\delta_\ell = \ell_2 - \ell_1$. Similarly, the field may be invariant under parity, which in two dimensions corresponds to an invariance under the flip of one of the axes of an image. This symmetry expresses that a clockwise and an anticlockwise rotation cannot be distinguished. When this invariance holds on top of rotational invariance, the WPH moments only depends on $|\delta\ell| = |\ell_2 - \ell_1|$.

The matter density field from Quijote simulations is expected to be invariant under translations, rotations, and parity. These symmetries allows to build parity-invariant WPH moments, which are labeled C^{isopar} . Describing the WPH moments of Eq. (7) in terms of oriented scales (j_i, ℓ_i) rather than frequencies $\vec{\xi}_i$ ⁴, one simply has:

$$C_{j_1, p_1, j_2, p_2, \delta\ell}^{\text{isopar}}(\vec{\tau}) = \left\langle C_{j_1, \ell_1, p_1, j_2, \ell_2, p_2}(\vec{\tau}) \right\rangle_{|\ell_2 - \ell_1| = |\delta\ell|} \quad (9)$$

where the angle brackets stand here for an angular average. These invariant moments offer a significant reduction of the dimension of WPH statistics, which reduces the variance of their estimators.

Parameter	Ω_m	Ω_b	h	n_s	σ_8
$\theta_\alpha^{\text{fid}}$	0.3175	0.049	0.6711	0.9624	0.834
$\Delta\theta_\alpha$	0.01	0.002	0.02	0.02	0.015

TABLE I: Fiducial values $\theta_\alpha^{\text{fid}}$ and finite deviations $\Delta\theta_\alpha$ of cosmological parameters used in simulations.

Discretization of spatial shift and spectral resolution. Since a convolved field $\rho * \psi_{\vec{\xi}_i}$ has been filtered at a 2^{j_i} scale, little or no additional information is gained from sampling it at a finer scale. To keep in line with the discretized wavelet approach, we consider only a discrete set of translations $\vec{\tau}$. Different sets of translations may be considered depending on the application (see App. A). Using non-zero values for the spatial shift $\vec{\tau}$ improves the spectral resolution beyond the spectral support of the wavelets but increases the number of WPH moments. A trade-off between the number of WPH moments and the spectral resolution must be sought, see Sec. V A for discussion.

WPH statistics used in this paper. We shall call *WPH statistics* a collection of some WPH moments (7) considered jointly. Defining WPH statistics amounts to selecting a set of $\{\vec{k}_1, p_1, \vec{k}_2, p_2, \vec{\tau}\}$ parameters as well as a set of symmetries (such as rotational invariance, parity, etc.). These choices can be adapted to the particular field under study. The specific WPH statistics used in this paper, either to estimate Fisher information about cosmological parameters in Sec. III or to produce realistic statistical syntheses in Sec. IV, are described in Appendix A. Our moment selection has been based not only on numerical experiments but also on the physical interpretation of the WPH moments as discussed in Sec. V.

III. FISHER INFORMATION ON COSMOLOGICAL PARAMETERS

We evaluate in this section the ability of WPH statistics to infer cosmological parameters by computing their Fisher information with respect to five cosmological parameters for 2D matter density fields from the Quijote simulations. First, we present the Quijote simulations and the density fields used, as well as the Fisher analysis that is performed. Then, we show how our results compare to state-of-the-art results obtained with usual summary statistics such as standard power spectrum, as well as joint power spectrum and bispectrum.

A. Quijote simulations

The physical LSS fields we study in this paper is the spatial distribution of the underlying matter density field, $\rho(\vec{x})$. We obtain these fields from the Quijote simulations of the Large Scale Structure of the Universe [22]. The Quijote simulations

³ Indeed, $\|[z]^p - [z']^p\| \leq \max(|p|, 1)|z - z'|$. See [19].

⁴ Meaning that a given $C_{j_1, \ell_1, p_1, j_2, \ell_2, p_2}$ matches the $C_{\vec{\xi}_1, p_1, \vec{\xi}_2, p_2}$ moment whose $\vec{\xi}_i$ correspond to the pairs (j_i, ℓ_i) , as given in Eq. (2).

are a set of 43,100 full N-body simulations of the LSS tracing the evolution of spatial fluctuations from redshift $z = 127$ to $z = 0$. Thousands of different cosmological models are simulated. The initial conditions at $z = 127$ are computed using 2LPT with CAMB [23], while the dynamic of the simulations that follows the evolution of the dark matter particles relies on the TreePM+SPH code Gadget-III, an improved version of Gadget-II [24]. We refer the reader to [22] for further details on these simulations.

In this paper, we use 2D matter fields of 256×256 pixels. These slices have been generated as follows: first, for each realization, a 3D density field with 256^3 voxels is computed by assigning particle positions to a the grid using the cloud-in-cell mass assignment scheme. Next, a slice with $256 \times 256 \times 64$ is taken and is projected (we compute the average) along the third axis. These fields represent a regions with an area equal to $1000 \times 1000 (h^{-1} \text{Mpc})^2$. The matter density fields $\rho(\vec{x})$ are normalized, which mean that they all verify $\bar{\rho} = 1$. In the following section, both the matter density field and its logarithm are studied. An example of such a field is given in Fig. 3.

We consider different cosmologies with five varying cosmological parameters. These parameters are respectively the matter density parameter, Ω_b the baryon density parameter, h the dimensionless Hubble parameter, n_s the scalar spectral index, and σ_8 the average rms matter fluctuation smoothed at $8h^{-1} \text{Mpc}$ scale. They are represented collectively as θ_α .

Two different sets of simulations are used in this paper. A first set contains 15000 simulations at Planck fiducial cosmology [25], for cosmological parameters $\theta_\alpha^{\text{fid}}$. A second set of simulations has been devised to numerically compute partial derivatives of the statistical descriptors used with respect to the different cosmological parameters. For each cosmological parameter θ_α , this set contains 500 simulations for $\theta_\alpha^{\text{fid}} \pm \Delta\theta_\alpha$, the other parameters being held fixed at the fiducial values (see [22] for more details). Values of $\theta_\alpha^{\text{fid}}$ and $\Delta\theta_\alpha$ are given in Table. I. Thus, we use 15,000 simulations to compute the covariance matrix, and 1,000 simulations per parameter to compute derivatives.

B. Fisher matrix analysis

The information about cosmological parameters θ_α contained —on average— in a given set of statistics can be quantified by computing the associated Fisher information matrix. Let consider a set $\{\Phi_1(\rho), \dots, \Phi_d(\rho)\}$ of d scalar statistics (such as WPH moments, for instance) computed from a realization ρ of the field. We denote $\mu_i(\theta_\alpha)$ the expected value of $\Phi_i(\rho)$ and $\Sigma_{ij}(\theta_\alpha)$ the covariance of $\Phi_i(\rho)$ and $\Phi_j(\rho)$ when ρ is drawn under θ_α . If the statistics are jointly Gaussian and if their covariance matrix Σ does not depend on θ_α , the Fisher information matrix boils down to [26]

$$F_{\alpha\beta} = \sum_i \sum_j \frac{\partial \mu_i}{\partial \theta_\alpha} (\Sigma^{-1})_{ij} \frac{\partial \mu_j}{\partial \theta_\beta}. \quad (10)$$

From this Fisher matrix, one can compute the Cramr-Rao bound, which gives the asymptotically lowest possible variance

Φ	P_k	$P_k + B_k$	WPH	P'_k	$P'_k + B'_k$	WPH'
Size	127	313	327	127	313	327
Ω_m	0.15	0.12	0.11	0.15	0.12	0.10
Ω_b	0.16	0.12	0.075	0.12	0.097	0.064
h	1.5	1.1	0.71	0.99	0.78	0.50
n_s	0.74	0.52	0.20	0.25	0.20	0.11
σ_8	0.024	0.013	0.018	0.012	0.0097	0.0097

TABLE II: Marginalized errors on cosmological parameters obtained with Fisher analysis. The different statistics used are power spectrum (P_k), joint power spectrum and bispectrum ($P_k + B_k$), and WPH statistics (WPH). These results are obtained with the matter density field (columns 2 to 4), and its logarithm (labelled with a prime, column 5 to 7).

$\delta\theta_\alpha^2$ for any unbiased estimator of θ_α based on Φ :

$$\delta\theta_\alpha \geq \sqrt{(F^{-1})_{\alpha\alpha}}. \quad (11)$$

In this paper, we numerically estimated the Fisher matrices for the cosmological parameters θ_α corresponding the Planck fiducial cosmology. We estimated the covariance matrix from the 15000 simulations for the Planck fiducial cosmology, while each partial derivative appearing in Eq. (10) is evaluated with the two sets of 500 simulations at $\theta_\alpha^{\text{fid}} \pm \Delta\theta_\alpha$ (see Table. I). For the computation of Fisher matrices, we checked the convergence by verifying that the results were only modified at the percent level when using 10000 (respectively, 350) simulations to compute the covariance matrices (respectively, the partial derivatives).

C. Fisher matrix results

We compare in this section the results obtained with three sets of summary statistics: the standard power spectrum, the power spectrum plus a set of bispectrum triangles, and a set of WPH statistics. The bispectrum triangle ensemble is described in App. B 2, and spans representative configurations of flattened, squeezed, and equilateral triangles. The WPH statistics, that contain 327 coefficients, are constructed from WPH moments given in Eq. (9) and which are invariant under rotations and parity. A complete description of these moments, that characterize all the scales of the image, is given in App. A 1.

For each of these descriptors, we show posterior distributions of the cosmological parameters by using the matter density field from Quijote simulations. We also show the same results based on the logarithm of the matter density field (labeled by an extra tick mark ') because we expect this non-linear

Φ	WPH	+ P_k	+ B_k	WPH'	+ P'_k	+ B'_k
Size	327	454	513	327	454	513
Ω_m	0.11	0.11	0.10	0.102	0.096	0.094
Ω_b	0.075	0.073	0.070	0.064	0.063	0.062
h	0.71	0.68	0.65	0.50	0.50	0.48
n_s	0.20	0.20	0.19	0.11	0.11	0.11
σ_8	0.018	0.018	0.0095	0.0097	0.0096	0.086

TABLE III: Marginalized errors on cosmological parameters obtained with the Fisher analysis. The different statistics used are WPH statistics (WPH), joint WPH statistics and power spectrum (+ P_k), and joint WPH statistics and bispectrum (+ B_k). These results are obtained with the matter density field (columns 2 to 4), and its logarithm (labelled with a prime, column 5 to 7).

that, with the exception of σ_8 for the bispectrum, only limited additional information is gained by adding these statistics to those built on WPH moments.

Joint power spectrum and bispectrum studies of various LSS fields have been performed in numerous works [e.g., 2]. Bispectrum forecasts for full sets of cosmological parameters have for instance been performed in [30–32]. In particular, the full information content of the redshift-space halo bispectrum for six cosmological parameters has been computed from the N-body Quijote simulations in [3]. However, the particular two-dimensional projected matter density field used in this paper makes difficult any quantitative comparison with the results obtained in those works. A similar analysis has also been performed for weak-lensing surveys by [33] with improvements from power spectrum to joint power power spectrum and bispectrum similar to those of the present paper. Given the widespread use of bispectrum in cosmological parameter inference, the present bispectrum results can then be taken as a generic benchmark. We thus claim that the results obtained with WPH statistics favorably compare to state-of-the-art results obtained with these other summary statistics. A more quantitative comparison is deferred to later work, since it requires WPH statistics to be extended to 3D fields.

IV. STATISTICAL SYNTHESSES WITH WPH STATISTICS

In this section, we show that WPH statistics embed a wide range of summary statistics commonly used in cosmology. For that purpose, we estimate WPH statistics on a subset of Quijote simulation maps, and generate from them synthetic maps based on a microcanonical maximum entropy principle. These syntheses are then compared to the whole sample of Quijote

maps by means of summary statistics commonly used in astrophysics such as power spectrum, bispectrum, probability distribution function (PDF), or Minkowski functionals.

First, we discuss the practical implementation of a microcanonical maximum entropy model used to statistically generate new realizations of a given random process. We then report the results obtained for the logarithm of the matter density field of the LSS Quijote simulations and show how they compare to state-of-the-art results obtained with other methods. Notice that previous studies, based on either WPH statistics [20, 22] or on the related Wavelet Scattering Transform [WST, 34–36], have considered similar syntheses. Their results were assessed only qualitatively, mostly from visual inspection. In contrast, Sect. IV B below reports much more stringent quantitative tests based on a wide set of statistics commonly used in astrophysics.

A. Microcanonical maximum entropy model

This section presents a generative algorithm for drawing sample realizations of a microcanonical maximum entropy model.

Maximum entropy models are obtained as probability distributions p which satisfy a set of statistical constraints, while being *as general as possible*, in the sense of maximizing the Shannon entropy $H(p) = - \int p(\rho) \log [p(\rho)] d\rho$. In this paper, we consider microcanonical models, which are defined as follows. Let $\tilde{\rho}$ denote a realization of the process under study and let $\Phi(\tilde{\rho})$ be a set of statistics computed on this realization. The microcanonical set Ω_ε of width ε conditioned by $\tilde{\rho}$ is defined as

$$\Omega_\varepsilon = \{\rho : d[\Phi(\rho), \Phi(\tilde{\rho})] \leq \varepsilon\}, \quad (12)$$

where $d[\Phi(\rho), \Phi(\tilde{\rho})]$ is a measure of discrepancy between $\Phi(\rho)$ and $\Phi(\tilde{\rho})$. The microcanonical maximum entropy model is the model of maximal entropy defined over Ω_ε , which implies that it has a probability distribution which is uniform on Ω_ε . We refer the reader to [37] and [20] for detailed explanations and for the exact definition of $d[\Phi(\rho), \Phi(\tilde{\rho})]$.

One can sample from microcanonical maximum entropy models using Monte-Carlo techniques, but such methods tend to be quite computationally expensive for a large number of statistical constraints [38]. For that reason, we rely on a different approach, introduced in [37]. To produce one realization of the microcanonical model, one starts from a realization ρ of an homogeneous and isotropic Gaussian field which is then modified iteratively by descending the loss function $\mathcal{L} = d[\Phi(\rho), \Phi(\tilde{\rho})]$. Care must be taken that the descent preserves the key symmetries of the starting point: homogeneity and isotropy.

For this paper, the microcanonical maximum entropy sampling is implemented in Python using the PyTorch library [39] to compute the gradient of the loss and the loss descent is performed using the L-BFGS-B[40] implementation of Scipy [41].

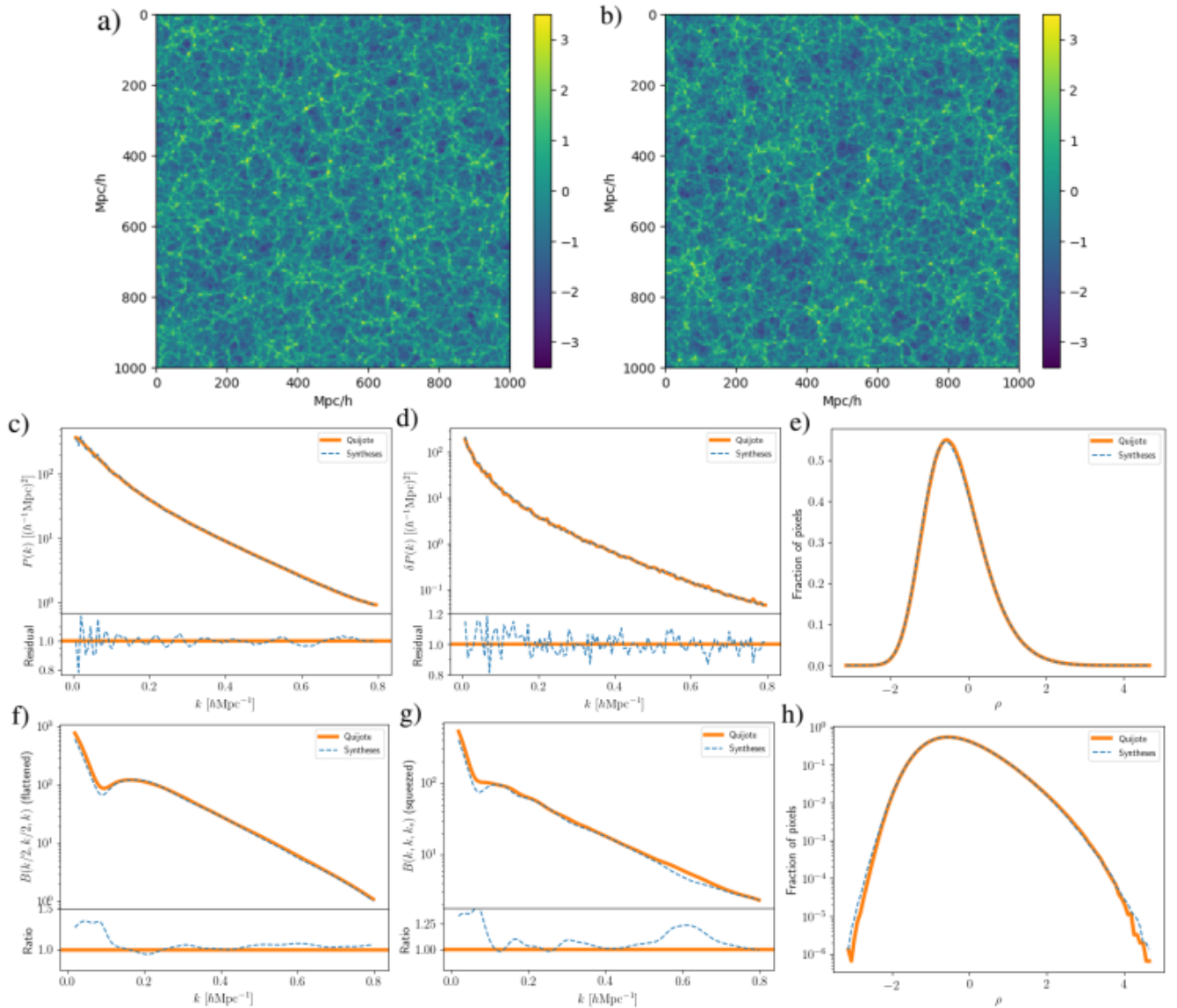


FIG. 5: Comparison between the logarithm of Quijote matter density field and its syntheses. a) A map from the Quijote simulation. b) A map synthesized by the algorithm of section IV A. c) Power spectrum of the Quijote simulation (thick orange line) and of the syntheses (blue dashed line). d) Standard deviation of the power spectrum of the Quijote simulation (thick orange line) and of the syntheses (blue dashed line). e) Pixel value PDF of the Quijote simulation (thick orange line) and of the syntheses (blue dashed line) in linear scale. f) Bispectra $B(k_1, k_2, k_3)$ in the flattened triangle configuration, i.e. with $k_2 = k_3 = k_1/2$ as a function of k_1 . The orange thick line corresponds to the Quijote maps and the dashed blue line to the syntheses. g) Bispectra $B(k_1, k_2, k_3)$ in the squeezed triangle configuration, i.e. with $k_1 = k_2$ and $k_3 \ll 1$ as a function of k_1 . The orange thick line corresponds to the Quijote maps and the dashed blue line to the syntheses. h) Pixel value PDF of the Quijote simulation (thick orange line) and of the syntheses (blue dashed line) in logarithmic scale. All the statistics presented in this figure have been estimated using 300 maps from Quijote and 300 syntheses. This figure displays how well the syntheses reproduce the statistical properties of the logarithm of Quijote maps.

B. Statistical validation of the syntheses

In this section, we assess the quality of the syntheses generated by the maximal entropy model. Rather than working with the matter density field itself, we chose to work with its logarithm. Indeed, as the matter density field roughly follows

a log-normal distribution, its logarithm follows a normal distribution, and we found that it was better reproduced by our maximal entropy model.

The WPH statistics used in this section, and detailed in App. A 2, contain 6676 coefficients. These coefficients do not implement invariance under rotations, and are constructed from

Eq. (7) rather than Eq. (9). This explains the increase in the number of coefficients with respect to the WPH statistics used in Sec. III. We found out that this choice leads to better syntheses. We believe this is due to the fact that the Cartesian grid breaks the rotational symmetry, especially at small scales. The other difference is that the scales above $J = 6$ are constrained by low-pass filters rather than WPH moments, see App A 2 for more details.

To implement the method described above, we estimated the WPH statistics following Eq. (7) from several 1 (Gpc/h)² maps of 256×256 pixels with periodic boundary conditions. We found empirically that 30 maps were sufficient to properly estimate the WPH coefficients up to those scales, and accordingly generate synthetic Quijote maps by batches of 30 syntheses. From the same 30 initial maps, we generated 300 syntheses (i.e. 10 batches of 30 syntheses), which took about 50 GPU hours⁵. Fig. 5 shows one map from the Quijote simulation and one synthesized map.

To assess the quality of the syntheses, we compute some n -point statistics for $n = 1, 2, 3, 4$ on the syntheses and compare them to the values of the initial Quijote maps. These statistics (and all the results shown in this section) are estimated using 300 Quijote maps and 300 synthetic maps. For $n = 1$, we compare the pixel distributions; for $n = 2$ and $n = 3$, we compare power spectra and bispectra; for $n = 4$, we compare the standard deviation and the correlation matrix of the empirical power spectrum. These results, together with histograms of power spectrum coefficients at three different frequencies, are presented in Figs. 5 and 7.

For isotropic homogeneous fields, the bispectrum is defined by three wave-vectors ($\vec{k}_1, \vec{k}_2, \vec{k}_3$) satisfying the triangle inequalities, and therefore representing the lengths of the edges of a triangle. We focused on three triangle configurations: squeezed triangles ($\vec{k}_1 \simeq \vec{k}_2$ and $k_3 \ll k_1$), flattened triangles ($\vec{k}_1 = \vec{k}_2 = \vec{k}_3/2$), and equilateral triangles ($k_1 = k_2 = k_3$). The results for flattened and squeezed triangles are given in Fig. 5, those for equilateral triangles are shown in Fig. 6. Bispectrum computation is described in appendix B 2.

We finally computed the Minkowski Functionals (MFs) of the syntheses. These are statistics capturing the topology of the level sets of the field. They have been used in cosmology to probe the non-Gaussianity of the CMB [42], to probe departures from General Relativity from the LSS [43], or to study lensing convergence maps [44]. In 2 dimensions, there are 3 MFs that depend on a threshold ν , and are noted $V_0(\nu)$, $V_1(\nu)$ and $V_2(\nu)$. Their definitions are recalled in appendix B 3. The MFs of the syntheses are shown in figure 7.

These different results show that the syntheses from WPH statistics presented in this section perform remarkably well in reproducing the statistical properties of the logarithm of the Quijote LSS matter density field. Indeed, the mean of the empirical power spectrum, its standard deviation, and its correlation are reproduced to within 5%, 10%, and 10%, respectively. The squeezed and flattened bispectra are reproduced to

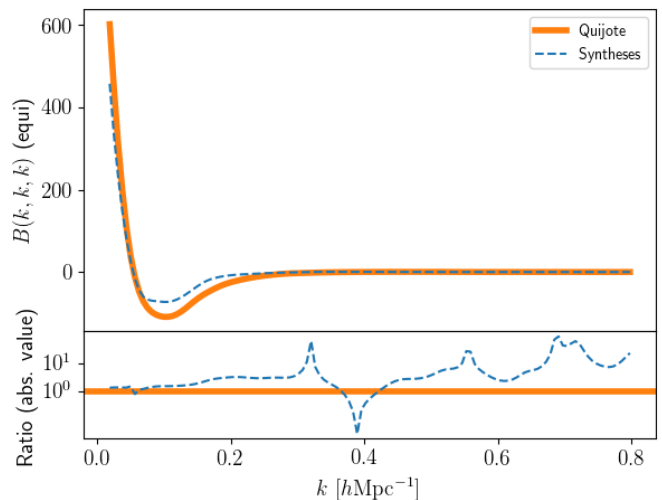


FIG. 6: Equilateral configuration of the bispectrum for the Quijote simulations (orange line) and syntheses (dark blue). As in previous figures, both bispectrum results have been computed using 300 maps.

within 10% and 20%, respectively, at spatial frequencies larger than $k = 0.1 \text{ hMpc}^{-1}$, and to within 40% below this spatial frequency. The whole probability distribution function is also very well reproduced, including the tails up to 4 orders of magnitudes in density. To compare our results to those obtained with GANs in generating astrophysical fields [45], we also show in Fig. 7 the distribution of the empirical power spectrum at three wavenumbers with no visible discrepancy from Quijote. Finally, the three MFs are respectively reproduced to within 0.5%, 0.05% and 0.02%.

Note that the equilateral bispectra (cf Fig. 6) is not well reproduced by the syntheses even though its general shape and its changes of sign are reproduced. This results can however be related to the fact that such bispectrum configurations corresponds to correlation between three clearly separate frequencies, and thus cannot be directly characterized by moments of two wavelet convolutions only. To extend the WPH construction to the characterization of such couplings is left to future work. It is however worth noticing that maximum-entropy syntheses manage to reproduce the general shape of such bispectrum triangles, albeit not very accurately.

Previous works based on convolutional neural networks, and especially on Generative Adversarial Networks (GANs) have produced syntheses of astrophysical fields. For example, [46] used a GAN to emulate accurate high-resolution features from computationally cheaper low-resolution cosmological simulations. Similarly, in [45], the authors used GANs to generate maps representing the *interstellar medium* (ISM). More recently, [47] trained GANs to reproduce both weak lensing convergence maps and dark matter over-density fields. In all these works, the quality of the syntheses is assessed as in the present paper, i.e. by computing histograms, power spectra, bispectra and Minkowski functionals, and we find results of similar quality.

As our method relies on the explicit construction of statistics,

⁵ The GPU used was a GPU Nvidia Tesla P100 with 16Go of RAM.

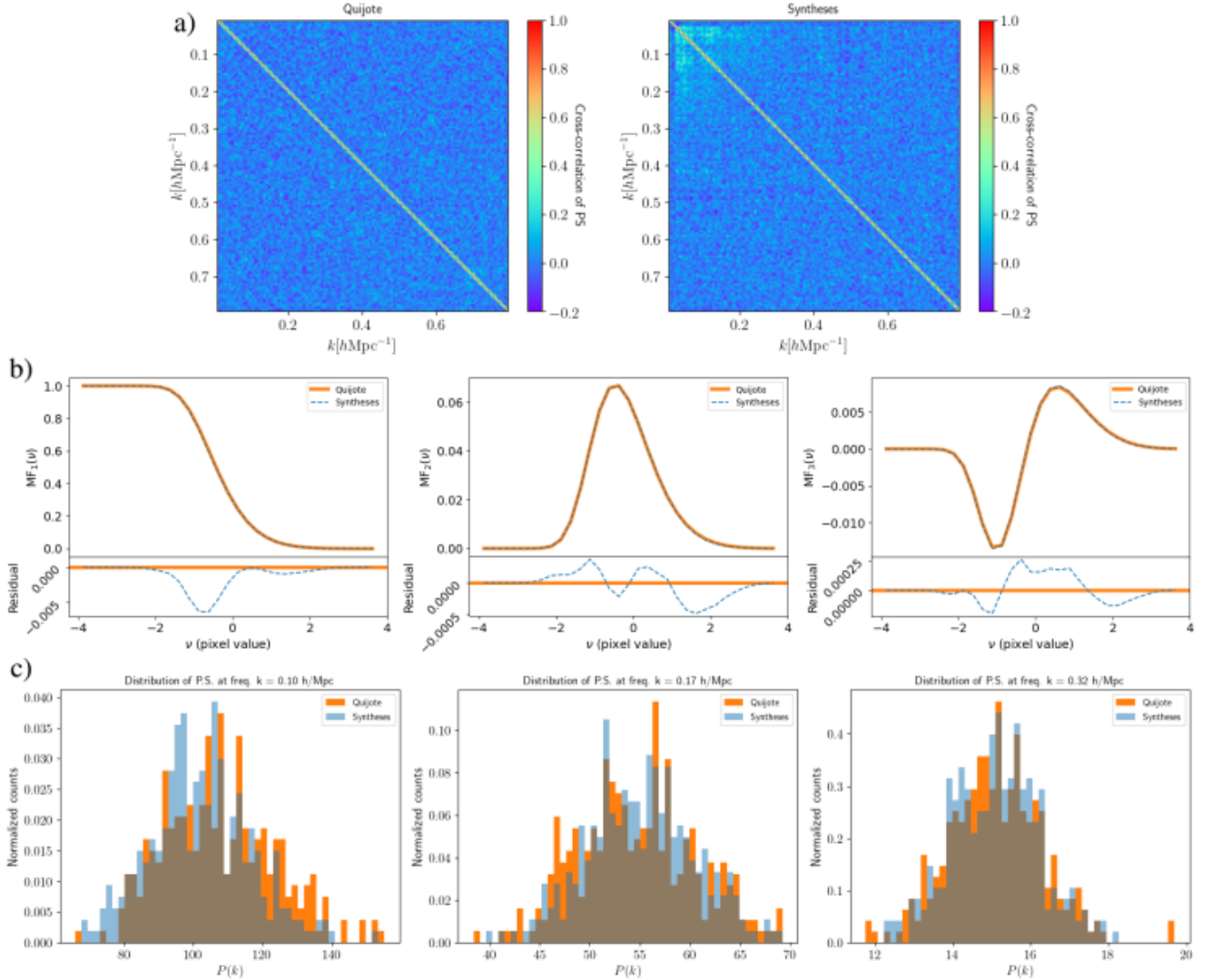


FIG. 7: Comparison between the logarithm of Quijote maps and its syntheses. Panels a: Correlation matrix of the power spectrum of respectively the Quijote maps (left) and of the syntheses (right). Panels b: First, second and third Minkowski functionals of the Quijote maps (thick orange line) and the syntheses (dashed blue line). Panels c: Histograms of the distribution of the power spectrum, respectively at the frequencies $k = 0.1\text{h/Mpc}$, $k = 0.32\text{h/Mpc}$ and $k = 0.17\text{h/Mpc}$ for the Quijote maps (orange) and the syntheses (blue). All the statistics shown in these figures are estimated using 300 Quijote maps and 300 syntheses. This figure displays how well the syntheses reproduce the statistical properties of the logarithm of Quijote maps.

it is not subject to the usual caveats of neural network methods. First of all, the WPH statistics can be physically interpreted (cf section V). Secondly, neural network methods require to learn a large amount of parameters (weights) from a huge training dataset, while we only use 30 initial Quijote maps for our syntheses. Also, using GANs to generate new realizations of a given process, one might suffer from mode collapse, *i.e.*, the omission of certain object classes in the generated images, as well as the associated statistical features [48]. This underlines the advantages of maximum entropy syntheses using a well defined tailored statistical description as the WPH moments.

V. PHYSICAL INTERPRETATION OF THE WPH STATISTICS

This section discusses the physical meaning of the various WPH moments as well as their relation to other summary statistics. It complements the discussion of symmetries of Sec. II D.

To identify the physical properties encoded in the WPH moments, we distribute these moments in a few categories, which are defined by selecting a set of $\{\xi_1, p_1, \xi_2, p_2\}$ parameters. Some of these categories are described by a single ξ_1 spectral wavelet band (see Sec. V A), while others describe a coupling between two wavelet bands of central frequencies ξ_1

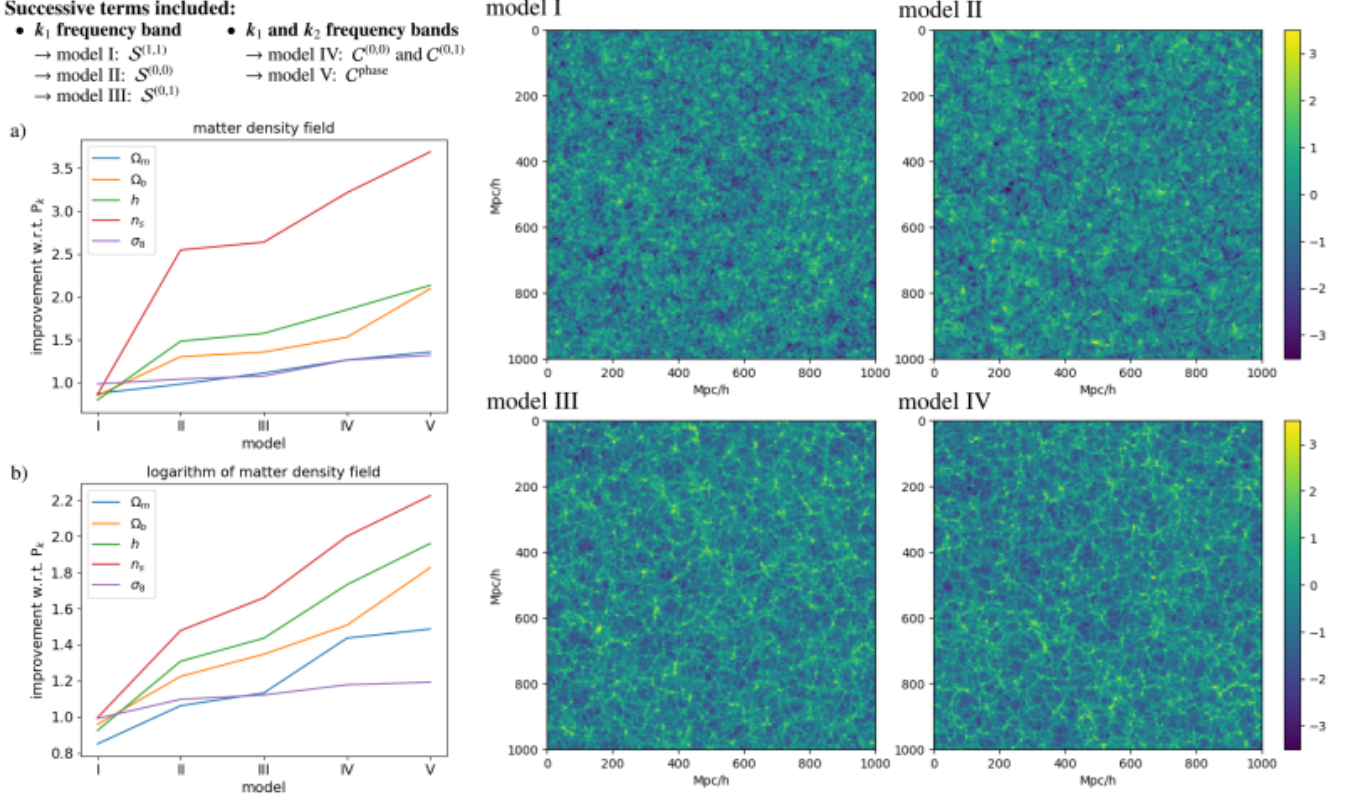


FIG. 8: Left: Marginalized errors on cosmological parameters obtained with Fisher analysis for models I to V of WPH statistics, with projected matter density field (a) and its logarithm (b). Right: Syntheses of the logarithm of the matter density field for model I to IV of WPH statistics. This figures illustrates the improvement of the results obtained from model I to model V.

and $\vec{\xi}_2$ (see Sec. VB). To study these different categories of moments, we progressively include them in our analysis, while building what we call model I to model V. For these different models, we compute Fisher information and perform statistical syntheses⁶. While model I merely contains power spectrum information, model V corresponds to WPH statistics used in Sec. III and IV. The dependency on the spatial translation parameter $\vec{\tau}$ is also discussed.

A. Terms related to a single wavelet frequency band

Let us first consider WPH moments that describe a single spectral wavelet band. Starting from the moments $C_{\vec{\xi}_1, p_1, \vec{\xi}_2, p_2}(\vec{\tau})$ given in Eq. (7), we restrict ourselves to cases where $\vec{\xi}_1 = \vec{\xi}_2$. Hence, we focus on moments of the form

$$\mathcal{S}_{\vec{\xi}_1}^{(p_1, p_2)}(\vec{\tau}) = C_{\vec{\xi}_1, p_1, \vec{\xi}_1, p_2}(\vec{\tau}) \quad (13)$$

and we consider three such terms obtained for phase exponents (p_1, p_2) equal to (1, 1), (0, 0) or (0, 1). Explicitly, these are

$$\mathcal{S}_{\vec{\xi}_1}^{(1,1)}(\vec{\tau}) = \text{Cov}(\rho * \psi_{\vec{\xi}_1}(\vec{x}), \rho * \psi_{\vec{\xi}_1}(\vec{x} + \vec{\tau})), \quad (14)$$

$$\mathcal{S}_{\vec{\xi}_1}^{(0,0)}(\vec{\tau}) = \text{Cov}(|\rho * \psi_{\vec{\xi}_1}(\vec{x})|, |\rho * \psi_{\vec{\xi}_1}(\vec{x} + \vec{\tau})|), \quad (15)$$

$$\mathcal{S}_{\vec{\xi}_1}^{(0,1)}(\vec{\tau}) = \text{Cov}(|\rho * \psi_{\vec{\xi}_1}(\vec{x})|, \rho * \psi_{\vec{\xi}_1}(\vec{x} + \vec{\tau})). \quad (16)$$

Note that $\mathcal{S}^{(1,1)}$ corresponds to the covariance of wavelet transforms presented in Sec. II B.

Model I: $\mathcal{S}^{(1,1)}$ moments, power spectrum. As shown in Sec. II B, the $\mathcal{S}^{(1,1)}$ moments, that form model I WPH statistics, only depend on the power spectrum of ρ . This is illustrated by the fact that syntheses from model I generate fields close to Gaussian (see Fig. 8), which have for instance vanishing bispectra, as well as Gaussian PDF (see Fig. 10).

These moments also emphasize the impact of the number of relative spatial translations $\vec{\tau}$, which is parametrized by Δ_n , in the spectral resolution. This property is illustrated in Fig. 9, where the power spectrum of model I syntheses are given: imprints of the wavelet spectral bands are clearly visible when using $\vec{\tau} = 0$ only (which corresponds to $\Delta_n = 0$), while they are clearly reduced when several $\vec{\tau}$ values are retained, e.g. when $\Delta_n = 2$ (see App. A 2 for more details). Similar results are obtained for the Fisher analysis of cosmological parameters.

⁶ Note that as in Sec. IV, only syntheses of the logarithm of the LLS matter density field are performed, while the Fisher analysis is done for both the Quijote matter density field and its logarithm.

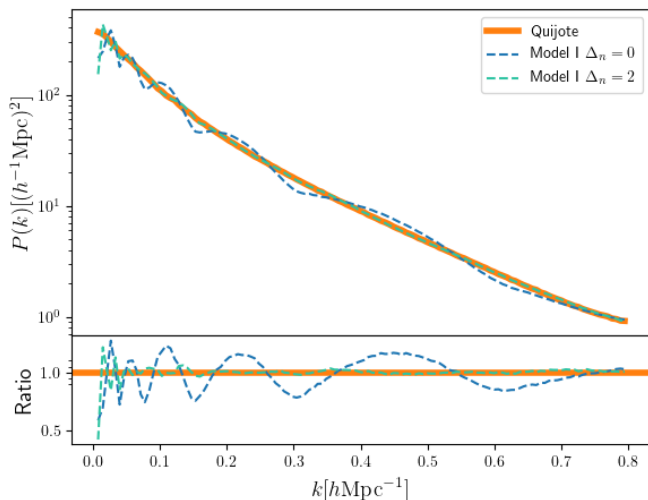


FIG. 9: Improvement of the power spectrum of the syntheses with respect to the number of \vec{z} translation used. These results are obtained using model I, and thus WPH coefficients that characterize power spectrum information only. Δ_n corresponds to the maximum value of n used in in the spatial translation, as defined by Eq. A1. When $\Delta_n = 0$, no spatial translation \vec{z} is used.

Indeed, the amount of information on cosmological parameters of model I WPH statistics increases with the number of retained values of \vec{z} , eventually converging to the information contained in the standard power spectrum.

Model II: $\mathcal{S}^{(0,0)}$ moments and sparsity. The $\mathcal{S}^{(0,0)}$ moments, which complement model I to form model II WPH statistics, allow to quantify the ratio between the \mathbf{L}^1 and the \mathbf{L}^2 norms of the wavelet transform of ρ . Such a quantity characterizes the sparsity of the field in the wavelet basis [see 20, for a more detailed discussion]. In the Quijote LSS simulations, these coefficients indicate that the small scales are sparser than the large ones, whose sparsity converges to that of a Gaussian field. Such a result is expected, since the LSS density fields are expected to become Gaussian at scales larger than $100 \text{ Mpc}/h$.

These moments significantly increase the amount of Fisher information about the cosmological parameters with respect to model I, see Fig. 8. A substantial increase of Fisher information is also obtained while considering several spatial shifts \vec{z} , similarly to $\mathcal{S}^{(1,1)}$ moments. In contrast, the $\mathcal{S}^{(0,0)}$ moments do not substantially improve the synthesis results, as can be seen in the right hand side panels of Fig. 8.

Model III: $\mathcal{S}^{(0,1)}$ moments and first structures. To build the third model of WPH statistics, we add the $\mathcal{S}^{(0,1)}$ moments to model II. Since they measure a covariance between wavelets coefficients which undergo two different operations (namely, modulus and identity), these terms mainly describe couplings between different spatial frequencies within a single wavelet band, see Sec. II C. They thus illustrate the impact of the interaction between neighboring scales in WPH statistics.

The $\mathcal{S}^{(0,1)}$ moments allow for a major improvement of the synthesis results obtained. This is illustrated in Fig. 8, where the familiar foamy structure of the LSS is recognized. This is

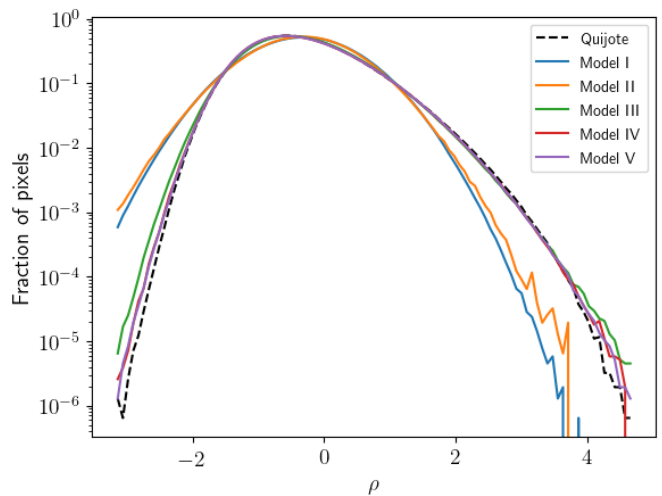


FIG. 10: Probability distribution function of the statistical syntheses of the logarithm of Quijote matter density field as performed with the WPH descriptions of model I to V. The PDF of the initial Quijote field is also given.

also illustrated in the PDF given in Fig. 10, which reproduces the main shape of the PDF of Quijote simulations. Similarly, the Minkowski functionals and the flattened bispectrum are also broadly reproduced, but not the squeezed bispectrum. This last result is understandable, since squeezed bispectrum triangles characterize the joint information between Fourier modes of wave-vectors of very different sizes.

In spite of these results, the improvement of the Fisher information about cosmological parameters is only minor. This is especially noticeable for the LSS matter density field, and less for its logarithm. These results emphasize that while the interactions between nearby scales are important statistics to qualitatively reproduce the web structure of the LSS, they do not seem efficient to discriminate between different cosmological parameter values.

B. Couplings between wavelet frequency bands

The second type of moments that we consider characterizes couplings between two wavelet spectral bands with central spatial frequencies \vec{k}_1 and \vec{k}_2 . We consider three kinds of such couplings, with different values of p_i . For each coupling term, we set $\xi_2 \leq \xi_1$ (which corresponds to spatial scales $2^{j_2} \geq 2^{j_1}$), without loss of generality. In each case, the values of p_i are chosen such that both phase harmonics of wavelet transforms appearing in Eq. (7) contain common spatial frequencies of oscillation. Similarly to the definition of Eq. 13, we define

$$C_{\xi_1, \xi_2}^{(p_1, p_2)}(\vec{\tau}) = C_{\xi_1, p_1, \xi_2, p_2}(\tau) \quad (17)$$

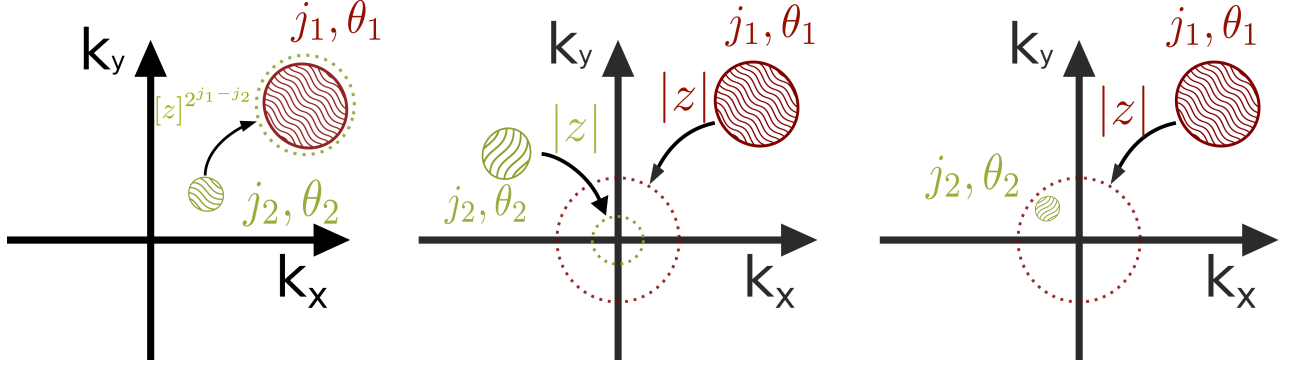


FIG. 11: Coupling terms in Fourier space. From left to right are pictured C^{phase} , $C^{(0,0)}$, and $C^{(0,1)}$ types of coupling. It is shown in each case how the frequency support of the filtered fields are modified by the phase harmonics in order to share common frequencies.

and we shall consider the moments obtained for $(p_1, p_2) = (0, 0)$ and $(p_1, p_2) = (0, 1)$. Explicitly, those are

$$C_{\vec{\xi}_1, \vec{\xi}_2}^{(0,0)}(\vec{\tau}) = \text{Cov} \left(\left| \rho * \psi_{\vec{\xi}_1}(\vec{x}) \right|, \left| \rho * \psi_{\vec{\xi}_2}(\vec{x} + \vec{\tau}) \right| \right) \quad (18)$$

$$C_{\vec{\xi}_1, \vec{\xi}_2}^{(0,1)}(\vec{\tau}) = \text{Cov} \left(\left| \rho * \psi_{\vec{\xi}_1}(\vec{x}) \right|, \rho * \psi_{\vec{\xi}_2}(\vec{x} + \vec{\tau}) \right). \quad (19)$$

For $\vec{k}_1 = \vec{k}_2$, the $C^{(0,0)}$ and $C^{(0,1)}$ moments are identical to $\mathcal{S}^{(0,0)}$ and $\mathcal{S}^{(0,1)}$ defined in the previous section. Note that $C^{(0,1)}$ is not symmetric under the exchange of $\vec{\xi}_1$ and $\vec{\xi}_2$, but that this term is negligibly small when $\xi_2 > \xi_1$, as discussed below.

These moments can be interpreted as follows. First, $C^{(0,0)}$ quantifies the correlation between local levels of oscillations at $\vec{\xi}_1$ and $\vec{\xi}_2$ spatial frequencies. Then, $C^{(0,1)}$ evaluates the correlation between the amplitude of the local level of oscillation at the $\vec{\xi}_1$ frequency and the oscillation at the $\vec{\xi}_2$ frequency. For this second moment, since $\rho * \psi_{\vec{\xi}_1}$ is filtered at a 2^{j_1} wavelength, it is clear that the correlation of its amplitude with a $\rho * \psi_{\vec{\xi}_2}$ term gives a negligible result if this second convolution oscillates at a characteristic scale $2^{j_2} < 2^{j_1}$.

The last type of couplings are for $(p_1, p_2) = (1, \xi_1/\xi_2)$, that is, they are of the form $C_{\vec{\xi}_1, \vec{\xi}_2}^{\text{phase}}(\vec{\tau}) = C_{\vec{\xi}_1, 1, \vec{\xi}_2, \xi_1/\xi_2}(\vec{\tau})$. We define:

$$C_{\vec{\xi}_1, \vec{\xi}_2}^{\text{phase}}(\vec{\tau}) = \text{Cov} \left(\rho * \psi_{\vec{\xi}_1}(\vec{x}), \left[\rho * \psi_{\vec{\xi}_2}(\vec{x} + \vec{\tau}) \right]^{\xi_1/\xi_2} \right). \quad (20)$$

For $\vec{k}_1 = \vec{k}_2$, this moment boils down to $\mathcal{S}^{(1,1)}$ defined in Eq. (14). The computation of such WPH moments is illustrated in Fig. 3, and has already been discussed in Sec. II C. Computed from fields filtered at different scales which are made synchronous, such terms are thus designed to characterize the relative phase shift between different scales.

These different coupling terms can also be understood from a Fourier space point of view. For each type of moments, Fig. 11 illustrates how the spectral supports of the ρ field after convolution by two wavelets, are modified by the phase harmonics operator. The three possible coupling terms correspond to various ways of achieving a (possibly partial) spectral overlap by band-passing followed by a phase multiplication.

Model IV & V: couplings between different wavelet bands. The final models of WPH statistics are built as follows. Model IV is built by adding the $C^{(0,0)}$ and $C^{(0,1)}$ moments to model III, and model V is finally built by then adding the C^{phase} moments. Note that these models include terms for which \vec{k}_1 and \vec{k}_2 have the same norm but different orientations. Model V corresponds to the statistical descriptions used in Sec. III and IV.

Model IV allows for an important improvement of the syntheses, which give results close to what is presented in Sec. IV. The squeezed bispectrum triangles are reproduced, as well as the tails of the PDF (with results that are better than model III by a factor close to 5). This result underlines that $C^{(0,0)}$ and $C^{(0,1)}$ moments are related to couplings between scales that are far apart. In particular, the PDF result exhibits how the precise peaks distribution of the LSS seems to be related to the coupling between different scales that sum up together in a coherent way. On the contrary, model V does not grant any significant improvement for the syntheses with respect to model IV.

For parameter inference, it is shown in Fig. 8 how both models IV and V give a noticeable improvement of the forecast errors on cosmological parameters. It is especially noteworthy that these improvements are generally significantly larger than what is obtained with the local coupling added in model III. It is also interesting to see that while the C^{phase} moments play a minor role to reproduce standard statistics in syntheses, they do contain a substantial amount of information about cosmological parameters. This result could indicate that those WPH moments are not directly related to the summary statistics used to validate the syntheses.

Importance of the ratio between coupled scales. An important parameter while constructing a set of WPH statistics from an ensemble of WPH moments is $\Delta_j = j_{\text{max}} - j_{\text{min}}$, that quantifies the maximum scale difference being characterized statistically with WPH moments. Indeed, the ratio between such scales is $2^{j_{\text{max}}}/2^{j_{\text{min}}} = 2^{\Delta_j}$. Similarly, the ratio between the norm of the more distant spatial frequencies that are coupled is $\xi_1/\xi_2 = 2^{\Delta_j}$.

For non-linear physical processes, this parameter is of major importance. Indeed, non-linearity implies a statistical interac-

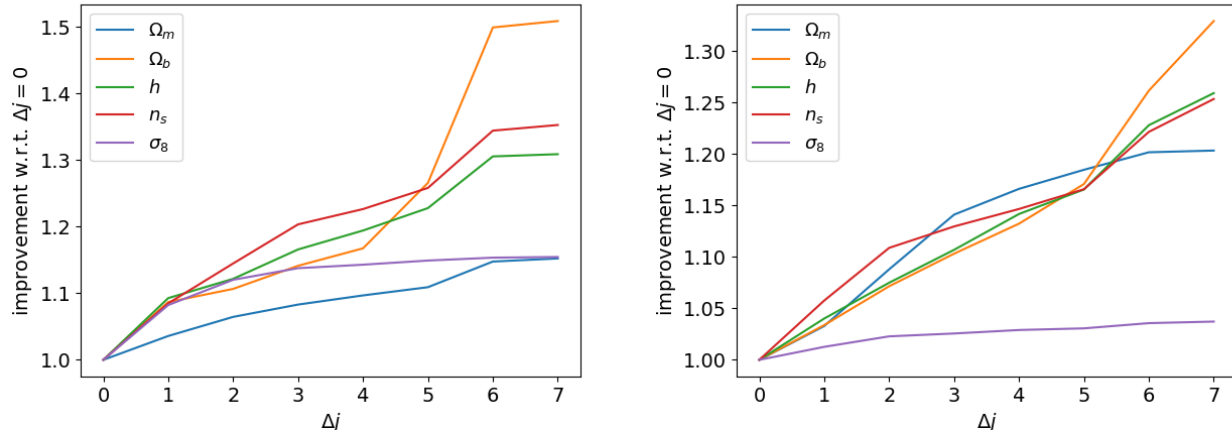


FIG. 12: Improvements of the marginalized errors on cosmological parameters obtained with Fisher analysis for model V of WPH statistics with increasing Δ_j values. These results, given for the LSS matter density field (left) and its logarithm (right), are normalized by the errors for $\Delta_j = 0$, for which only local couplings are characterized.

tion between different scales, and the more non-linear a given process is, the stronger we expect distant scales to be coupled [49]. We also expect different non-linear couplings to have distinct signatures in the way scales decouple from one another when the ratio between scales increases.

Let us illustrate the importance of the Δ_j parameter. For cosmological parameter inference, one can compute how the Fisher forecast errors evolve for model V with varying Δ_j . These results are given in Fig. 12, for errors that are normalized to the results obtained with $\Delta_j = 0$ (which corresponds to model III). It is clear in these results that significant information is contained in the coupling between different scales. One also see that adding the coupling with $\Delta_j \geq 5$, between scales which are very far apart (for example 2 and 64 pixels scales), still improve the Fisher results. This especially contrasts with

the minor improvements brought about by the inclusion of couplings between nearby scales.

Note that the increase of the Fisher information with Δ_j differs from one cosmological parameter to another. In particular, this improvement is only modest for Ω_m , and especially small for σ_8 . Also, Ω_m and σ_8 are the two parameters for which the WPH statistics does not characterize much more information than the power spectrum, see Tab. I. This indicates that these particular parameters do not especially modify the way distant scales couple. Note that this result seems rather natural for σ_8 , since this parameter is a mere normalization of the matter fluctuation power spectrum.

The importance of the Δ_j parameter also appears for the syntheses. Indeed, while the cosmic web structure visually appears when considering only local couplings with $\Delta_j = 0$ (see model II result in Fig. 8), it is necessary to take larger values of Δ_j to properly reproduce the tails of its PDF, which especially characterize the peak distribution of the LSS. This can be seen by comparing model III and model IV or V results in Fig. 10. Similarly, it is also necessary to consider larger values of Δ_j to reproduce the squeezed bispectrum triangles of the Quijote LSS field (see Fig. 12). This is however an expected result, since such triangles characterize couplings between very different scales.

VI. CONCLUSION

In this paper, we introduced low-dimensional Wavelet Phase Harmonics (WPH) statistics for analysis and synthesis of two-dimensional projected matter density fields from the Quijote LSS simulations. These statistics are built from WPH moments, that have been recently introduced in data science. Such WPH moments are constructed from the covariance of wavelet coefficients whose spatial frequencies are made synchronous by means of a specific non-linear operator called the phase harmonic operator.

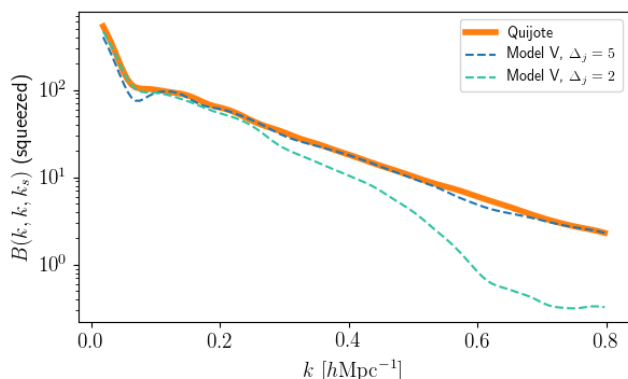


FIG. 13: Squeezed bispectrum of the logarithm of LSS matter density field of Quijote simulations and their syntheses from model V of WPH statistics with $\Delta_j = 2$ and $\Delta_j = 5$. This illustrates how the characterization of couplings between distant scales is necessary to reproduce the squeezed bispectrum of the LSS field.

The main result of this paper is the construction of low-dimensional WPH statistics which achieve state-of-the-art results both for their ability to capture cosmological information and to produce statistical syntheses. These results are obtained by computing the Fisher information of these statistics with respect to five cosmological parameters, and by producing maximum-entropy syntheses that are validated by means of classic summary statistics. To our knowledge, it is the first time that state-of-the-art results are obtained for both of these tasks from the same statistical description. We also illustrate the interpretability of WPH statistics by discussing which kind of information is described by the different WPH moments.

While WPH statistics are applied in this paper to projected LSS matter density field, their construction is not specific to this process. WPH statistics can thus be used to study other physical non-Gaussian fields. A natural extension is to three-dimensional fields which would allow a direct comparison with results obtained from other summary statistics or from machine learning methods.

Statistical syntheses from WPH statistics are mainly used in this paper as a validation tool. They can however serve as a generative model for various non-Gaussian fields. Example of applications are the generation of mock syntheses, as well as data augmentation for machine learning purposes. One of the advantages of these syntheses is that they can be performed from a limited training set, which could even be observational data.

Acknowledgments We thank D. Spergel, B. Mnard, and B. Wandelt, for fruitful discussions, as well as F. Levrier and B. Rgaldo-Saint Blancard for their comments on the draft. EA thanks the Flatiron Institute of Simons foundation for its generous hospitality during the preparation of this work. FVN acknowledges funding from the WFIRST program through NNG26PJ30C and NNN12AA01C. SM also acknowledges support from the PRAIRIE 3IA Institute of the French ANR-19-P3IA-0001 program.

Appendix A: Specifications of WPH models

1. Models for Fisher analysis

We present in this section the WPH statistics involved in Fisher analysis of Sec. III and Sec. V. These statistics are built from \mathcal{S} and \mathcal{C} moments defined in Sec. VA and VB. Assuming invariance under rotation and parity and following Eq. (9), we define from these terms invariant WPH moments called respectively $\mathcal{S}_{\text{isopar}}$ (that depend on an integer scale j_1) and $\mathcal{C}_{\text{isopar}}$ (that depend on two j_1 and j_2 integer scales and an absolute angle $\delta\ell$).

We consider only a discrete set $\{\tau_{n,\alpha}\}$ of spatial translations labeled by an integer n . Translation $\tau_{n,\alpha}$ is defined with respect to the wavelet $\psi_{j,\ell}$ of largest characteristic wavelength appearing in Eq. (7). It is oriented in the direction of oscillation of this wavelet, and is given by:

$$\tau_{n,\alpha} = n2^j \vec{e}_{(2\pi\ell/L)+\alpha}. \quad (\text{A1})$$

Note that these translations are redundant when larger than half of the size of the fields (128 pixels in this paper).

The WPH statistics of Sec. III have integer j values between 0 and 7, corresponding to characteristic scales from 2 to 256 pixels. Thus, all the scales of the matter density fields are characterized with WPH moments. These WPH statistics are also invariant under rotation and parity, and characterize couplings between all wavelet bands, with $\Delta j = 7$. They are defined as follows:

- For $\mathcal{S}_{\text{isopar}}^{(1,1)}$, $\mathcal{S}_{\text{isopar}}^{(0,0)}$ and $\mathcal{S}_{\text{isopar}}^{(0,1)}$ moments, we consider all j_1 values between 0 and 7. For each j_1 value, we consider all possible translation defined by eq. A1 with $\alpha = 0$ and $0 \leq n \leq \Delta_n$, with $\Delta_n(j_1) = [5, 5, 5, 5, 3, 1, 0, 0]$.
- For $\mathcal{C}_{\text{isopar}}^{(0,0)}$, $\mathcal{C}_{\text{isopar}}^{(0,1)}$ and $\mathcal{C}_{\text{isopar}}^{\text{phase}}$, we consider all (j_1, j_2) pairs in the form $0 \leq j_1 \leq j_2 \leq 7$. We take $2\pi\delta\ell/L \in [0, \pi/4, \pi/2]$ when $j_1 \in [0, 1]$, and $2\pi\delta\ell/L \in [0, \pi/2]$ otherwise. In addition, for $j_2 = 7$, we take only $\delta\ell = 0$. Finally, we consider translations $n = 0$ and $n = 1$ if $0 \leq j_1 = j_2 \leq 5$, and only $n = 0$ otherwise.

These WPH statistics contain a total of 327 WPH moments. In Sec. V, we measured the increase of Fisher information about cosmological parameters when the set of WPH moments was increased from model I to model V. Model I includes all the $\mathcal{S}^{(1,1)}$ terms, model II the $\mathcal{S}^{(1,1)}$ and $\mathcal{S}^{(0,0)}$ terms, etc. Table IV provides the number of WPH moments in each models.

Model index	I	II	III	IV	V
Model size	32	64	96	252	327

TABLE IV: Number of WPH moments in the nested models of Section V to perform Fisher analysis.

2. Models for statistical syntheses

This section presents the WPH statistics used to perform syntheses in Sec. IV, which corresponds to the model V in Sec. V. As in Sec. A1, we use the notations introduced in Sec. V, *i.e.*, \mathcal{S} and \mathcal{C} moments respectively defined in Sec. VA and VB.

The WPH statistics used in the syntheses of Sec. IV have integer j values between 0 and 5, corresponding to characteristic scales up to 64 pixels. They thus do not characterize in terms of WPH moments the largest scales of the matter density fields, but describe couplings between all scales studied, with $\Delta j = 5$. These WPH statistics are not invariant under rotation and parity, contrary to the WPH used for Fisher analysis. They are defined as follows:

- For $\mathcal{S}^{(1,1)}$, $\mathcal{S}^{(0,0)}$ and $\mathcal{S}^{(0,1)}$ moments, we consider all j_1 values between 0 and 5. For each j_1 value, we consider for $\mathcal{S}^{(1,1)}$ and $\mathcal{S}^{(0,0)}$ all possible translations defined by equation A1 with $0 \leq n \leq \Delta_n = 2$ and $\alpha \in \{-\pi/4, 0, \pi/4, \pi/2\}$. No translations are applied to $\mathcal{S}^{(0,1)}$.

- For $C^{(0,0)}$, $C^{(0,1)}$ and C^{phase} , we consider all j_1 values between 0 and 5, and all j_2 values between j_1 and 5. $\delta\ell = 0$ for C^{phase} and $|\delta\ell| \in \{0, 1, 2, 3, 4\}$ for $C^{(0,0)}$ and $C^{(0,1)}$. For $C^{(0,1)}$ and C^{phase} , when $\delta\ell = 0$ all possible translations defined by equation (A1) are applied for $0 \leq n \leq \Delta_n = 2$ and $\alpha \in \{-\pi/4, 0, \pi/4, \pi/2\}$.

To complete these WPH statistics and better constrain the scales that are not probed by WPH moments as well as the probability distribution function, we also consider convolutions of the field ρ with a family of low-pass filters $\varphi_j(\vec{x})$ called *scaling functions*. These low-pass filters are obtained by dilating an initial Gaussian window $\varphi(\vec{x})$:

$$\varphi_j(\vec{x}) = 2^{-j} \varphi(2^{-j} \vec{x}), \quad (\text{A2})$$

$$\hat{\varphi}_j(\vec{k}) = 2^j \hat{\varphi}(2^j \vec{k}), \quad (\text{A3})$$

where $\phi(\vec{x})$ is defined in App. B 1. We therefore added the following scaling moments $L_{j,p}$ to the WPH moments:

$$L_{j,0} = \text{Cov} [|\rho * \varphi_j|, |\rho * \varphi_j|], \quad (\text{A4})$$

$$L_{j,p} = \text{Cov} [(\rho * \varphi_j)^p, (\rho * \varphi_j)^p], \quad (\text{A5})$$

with j between 2 and 5 and $p \in \{0, 1, 2, 3\}$, yielding 16 scaling moments.

This model (model V) contains overall 6676 WPH moments. Note that the models I to V used in Sec. III for the syntheses do not use *isopar* coefficients, and therefore contain more terms than the models I to V used for the Fisher analysis.

Appendix B: Mathematical specifications

1. Bump steerable wavelets

We present in this appendix the mother wavelet ψ used to build the multi-scale bump-steerable wavelets $\psi_{j,\ell,n}$ in Sec. II A. The bump steerable wavelets were first introduced in [19], and were proven to be successful to synthesize various textures [20]. The bump steerable mother wavelet ψ is defined from its Fourier transform $\hat{\psi}(\vec{k})$ that yields:

$$\hat{\psi}(\vec{k}) = c \cdot \exp\left(\frac{-(\|\vec{k}\| - \xi_0)^2}{\xi_0^2 - (\|\vec{k}\| - \xi_0)^2}\right) \cdot \mathbf{1}_{[0,2\xi_0]}(\|\vec{k}\|) \times \cos^{L/2-1}(\arg(\vec{k})) \cdot \mathbf{1}_{[0,\pi/2]}(|\arg(\vec{k})|) \quad (\text{B1})$$

where $(\xi_0, 0)$ is the central frequency of the wavelet, c a normalization constant, L the number of angles used in the multi-scale wavelet family. We also used the indicator function $\mathbf{1}_A(x)$ that returns 1 if $x \in A$ and 0 otherwise. An example of bump-steerable wavelet is given in Fig. 2.

The low-pass filter ϕ used to construct the low-pass filtered $\phi_{j,n}$ is defined by its Fourier transforms as:

$$\hat{\phi}(\vec{k}) = \exp\left(-\frac{\|\vec{k}\|^2}{2\sigma^2}\right) \quad (\text{B2})$$

Following [20], we used $\xi_0 = 1.7\pi$, $\sigma = 0.248 \times 2^{-0.55} \xi_0$ and $c = 1.29^{-1} 2^{L/2-1} \frac{(L/2-1)!}{\sqrt{(L/2)(L-2)!}}$ with $L = 16$.

2. Bispectrum estimates

Regarding bispectrum computation, we have adapted the method described in [50] by which a smoothed isotropic bispectrum is estimated as a triple correlation between three filtered versions of the field.

In this method, we consider isotropic filters h_i which select only frequencies \vec{k} such that $\|\vec{k}\| = k_i$, and define $\rho_i = \rho * h_i$. The bi-spectrum at frequencies (k_1, k_2, k_2) is then estimated from $\mathbb{E} [\rho_1(\vec{x}) \rho_2(\vec{x}) \rho_3(\vec{x})]$

In particular, we use the following filters:

$$h_i(\vec{k}) = \frac{1}{\sigma \sqrt{2\pi}} \exp\left[-\frac{\|\vec{k} - \vec{k}_i\|^2}{2\sigma^2}\right]. \quad (\text{B3})$$

In the following, all wavenumbers are defined with respect to $k_N = 1/256 \text{ hMpc}^{-1}$. All bispectrum computations used to validate the syntheses in Sec. IV use $\sigma = 4k_N$.

The bispectrum statistics used in Sec. III to compute Fisher information about cosmological parameters are defined as follows:

- All flattened triangle configurations $B(k, k/2, k/2)$, with $k = (2n + 1) * k_N$ for n between 1 and 62.
- All equilateral triangle configurations $B(k, k, k)$, with $k = (2n + 1) * k_N$ for n between 1 and 62.
- All squeezed triangle configurations $B(k, k, k_s)$, with $k = (2n + 1) * k_N$ for n between 1 and 62, and with $k_s = 4 * k_N$.

This set contains 62 triangles of each type, for a total of 186 bispectrum terms. They are computed with $\sigma = 2k_N$.

3. Minkowski functionals

We provide in this appendix the definition of the Minkowski functionals (MFs), which we use to assess the quality of the syntheses in section IV B.

Given a threshold ν , these three MFs are respectively the area, the perimeter and the genus defined by this threshold. More precisely for a field $I(\vec{x})$ defined on an area A_{tot} , let us define $\Gamma_{<\nu} = \{x/I(x) < \nu\}$ and $\Gamma_{\leq\nu} = \{x/I(x) \leq \nu\}$. Let A_ν be the area of $\Gamma_{\leq\nu}$, S_ν its perimeter, $C_{<\nu}$ the number of connex components of $\Gamma_{<\nu}$ and $C_{>\nu}$ the number of components of $\Gamma_{>\nu}$. Then:

$$V_0(\nu) = \frac{A_\nu}{A_{tot}}, \quad V_1(\nu) = \frac{S_\nu}{A_{tot}}, \quad V_2(\nu) = \frac{C_{<\nu} - C_{>\nu}}{A_{tot}}. \quad (\text{B4})$$

- [1] E. Sefusatti, M. Crocce, S. Pueblas, and R. Scoccimarro, Cosmology and the bispectrum, *Phys. Rev.* **D74**, 023522 (2006), [arXiv:astro-ph/0604505 \[astro-ph\]](#).
- [2] J. Byun, A. Eggemeier, D. Regan, D. Seery, and R. E. Smith, Towards optimal cosmological parameter recovery from compressed bispectrum statistics, *Mon. Not. Roy. Astron. Soc.* **471**, 1581 (2017), [arXiv:1705.04392 \[astro-ph.CO\]](#).
- [3] C. Hahn, V.-N. Francisco, C. Emanuele, and S. Roman, Constraining m_ν with the bispectrum i: Breaking parameter degeneracies, arXiv preprint arXiv:1909.11107 (2019).
- [4] C.-T. Chiang, C. Wagner, F. Schmidt, and E. Komatsu, Position-dependent power spectrum of the large-scale structure: a novel method to measure the squeezed-limit bispectrum, *JCAP* **1405**, 048, [arXiv:1403.3411 \[astro-ph.CO\]](#).
- [5] A. Stuart, M. G. Kendall, *et al.*, *The advanced theory of statistics* (Griffin, 1963).
- [6] D. Obreschkow, C. Power, M. Bruderer, and C. Bonvin, A robust measure of cosmic structure beyond the power-spectrum: Cosmic filaments and the temperature of dark matter, *Astrophys. J.* **762**, 115 (2013), [arXiv:1211.5213 \[astro-ph.CO\]](#).
- [7] R. Wolstenhulme, C. Bonvin, and D. Obreschkow, Three-point phase correlations: a new measure of nonlinear large-scale structure, *Astrophys. J.* **804**, 132 (2015), [arXiv:1409.3007 \[astro-ph.CO\]](#).
- [8] M. Alpaslan *et al.*, Galaxy and mass assembly (gamma): Fine filaments of galaxies detected within voids, *Mon. Not. Roy. Astron. Soc.* **440**, L106 (2014), [arXiv:1401.7331 \[astro-ph.CO\]](#).
- [9] K. Ali, D. Obreschkow, C. Howlett, C. Bonvin, C. Llinares, F. O. Franco, and C. Power, Cosmological constraints from fourier phase statistics, *Mon. Not. Roy. Astron. Soc.* **479**, 2743 (2018), [arXiv:1806.10276 \[astro-ph.CO\]](#).
- [10] J. M. Bardeen, A. Szalay, N. Kaiser, and J. Bond, The statistics of peaks of gaussian random fields, *Astrophys. J.* **304**, 15 (1985).
- [11] A. Pisani, E. Massara, D. N. Spergel, D. Alonso, T. Baker, Y.-C. Cai, M. Cautun, C. Davies, V. Demchenko, O. Doré, *et al.*, Cosmic voids: a novel probe to shed light on our universe, arXiv preprint arXiv:1903.05161 (2019).
- [12] A. Cohen and R. D. Ryan, *Wavelets and multiscale signal processing* (Springer, 1995).
- [13] S. Mallat, *A wavelet tour of signal processing* (Elsevier, 1999).
- [14] J. Van Den Berg, *Wavelets in physics* (Cambridge University Press, 2004).
- [15] M. Farge, K. Schneider, O. Pannekoucke, *et al.*, Multiscale representations: fractals, self-similar random processes and wavelets, *Handbook of Environmental Fluid Dynamics* **2**, 311 (2010).
- [16] M. Farge and K. Schneider, Wavelet transforms and their applications to mhd and plasma turbulence: a review, *Journal of Plasma Physics* **81** (2015).
- [17] P. Flandrin, Wavelet analysis and synthesis of fractional brownian motion, *IEEE Transactions on information theory* **38**, 910 (1992).
- [18] Y. Meyer, F. Sellan, and M. S. Taqqu, Wavelets, generalized white noise and fractional integration: the synthesis of fractional brownian motion, *Journal of Fourier Analysis and Applications* **5**, 465 (1999).
- [19] S. Mallat, S. Zhang, and G. Rochette, Phase harmonic correlations and convolutional neural networks, arXiv preprint arXiv:1810.12136 (2018).
- [20] S. Zhang and S. Mallat, Maximum entropy models from phase harmonic covariances, arXiv preprint arXiv:1911.10017 (2019).
- [21] J. Zarka, L. Thiry, T. Angles, and S. Mallat, Deep network classification by scattering and homotopy dictionary learning, arXiv preprint arXiv:1910.03561 (2019).
- [22] F. Villaescusa-Navarro, C. Hahn, E. Massara, A. Banerjee, A. M. Delgado, D. K. Ramanah, T. Charnock, E. Giusarma, Y. Li, E. Allys, *et al.*, The quijote simulations, arXiv preprint arXiv:1909.05273 (2019).
- [23] A. Lewis, A. Challinor, and A. Lasenby, Efficient computation of CMB anisotropies in closed FRW models, *Astrophys. J.* **538**, 473 (2000), [arXiv:astro-ph/9911177 \[astro-ph\]](#).
- [24] V. Springel, The Cosmological simulation code GADGET-2, *Mon. Not. Roy. Astron. Soc.* **364**, 1105 (2005), [arXiv:astro-ph/0505010 \[astro-ph\]](#).
- [25] N. Aghanim, Y. Akrami, M. Ashdown, J. Aumont, C. Baccigalupi, M. Ballardini, A. Banday, R. Barreiro, N. Bartolo, S. Basak, *et al.*, Planck 2018 results. vi. cosmological parameters, arXiv preprint arXiv:1807.06209 (2018).
- [26] M. Tegmark, A. N. Taylor, and A. F. Heavens, Karhunen-loeve eigenvalue problems in cosmology: How should we tackle large data sets?, *The Astrophysical Journal* **480**, 22 (1997).
- [27] M. C. Neyrinck, I. Szapudi, and A. S. Szalay, Rejuvenating the matter power spectrum: restoring information with a logarithmic density mapping, *The Astrophysical Journal Letters* **698**, L90 (2009).
- [28] M. C. Neyrinck, I. Szapudi, and A. S. Szalay, Rejuvenating power spectra. ii. the gaussianized galaxy density field, *The Astrophysical Journal* **731**, 116 (2011).
- [29] E. Massara, F. Villaescusa-Navarro, S. Ho, N. Dalal, and D. N. Spergel, Using the marked power spectrum to detect the signature of neutrinos in large-scale structure, arXiv preprint arXiv:2001.11024 (2020).
- [30] E. Sefusatti, M. Crocce, S. Pueblas, and R. Scoccimarro, Cosmology and the bispectrum, *Physical Review D* **74**, 023522 (2006).
- [31] V. Yankelevich and C. Porciani, Cosmological information in the redshift-space bispectrum, *Monthly Notices of the Royal Astronomical Society* **483**, 2078 (2019).
- [32] A. Chudaykin and M. M. Ivanov, Measuring neutrino masses with large-scale structure: Euclid forecast with controlled theoretical error, *Journal of Cosmology and Astroparticle Physics* **2019** (11), 034.
- [33] W. R. Coulton, J. Liu, M. S. Madhavacheril, V. Böhm, and D. N. Spergel, Constraining neutrino mass with the tomographic weak lensing bispectrum, *Journal of Cosmology and Astroparticle Physics* **2019** (05), 043.
- [34] S. Mallat, Group invariant scattering, *Communications on Pure and Applied Mathematics* **65**, 1331 (2012), <https://onlinelibrary.wiley.com/doi/pdf/10.1002/cpa.21413>.
- [35] J. Bruna and S. Mallat, Invariant scattering convolution networks, *IEEE Transactions on Pattern Analysis and Machine Intelligence* **35**, 1872 (2013).
- [36] E. Allys, F. Levrier, S. Zhang, C. Colling, B. Regalado-Saint Blancard, F. Boulanger, P. Hennebelle, and S. Mallat, The rwst, a comprehensive statistical description of the non-gaussian structures in the ism, *Astronomy & Astrophysics* **629**, A115 (2019).
- [37] J. Bruna and S. Mallat, Multiscale sparse microcanonical models, arXiv preprint arXiv:1801.02013 (2018).
- [38] R. Lustig, Microcanonical monte carlo simulation of thermodynamic properties, *The Journal of chemical physics* **109**, 8816 (1998).
- [39] A. Paszke, S. Gross, S. Chintala, G. Chanan, E. Yang, Z. DeVito, Z. Lin, A. Desmaison, L. Antiga, and A. Lerer, Automatic

- differentiation in pytorch, openreview.net (2017).
- [40] R. H. Byrd, P. Lu, J. Nocedal, and C. Zhu, A limited memory algorithm for bound constrained optimization, *SIAM Journal on Scientific Computing* **16**, 1190 (1995), <https://doi.org/10.1137/0916069>.
- [41] P. Virtanen, R. Gommers, T. E. Oliphant, M. Haberland, T. Reddy, D. Cournapeau, E. Burovski, P. Peterson, W. Weckesser, J. Bright, S. J. van der Walt, M. Brett, J. Wilson, K. Jarrod Millman, N. Mayorov, A. R. J. Nelson, E. Jones, R. Kern, E. Larson, C. Carey, Í. Polat, Y. Feng, E. W. Moore, J. VanderPlas, D. Laxalde, J. Perktold, R. Cimrman, I. Henriksen, E. A. Quintero, C. R. Harris, A. M. Archibald, A. H. Ribeiro, F. Pedregosa, P. van Mulbregt, and S. . . Contributors, SciPy 1.0: Fundamental Algorithms for Scientific Computing in Python, *Nature Methods* <https://doi.org/10.1038/s41592-019-0686-2> (2020).
- [42] P. A. R. Ade *et al.* (Planck), Planck 2013 results. xxiii. isotropy and statistics of the cmb, *Astron. Astrophys.* **571**, A23 (2014), [arXiv:1303.5083 \[astro-ph.CO\]](https://arxiv.org/abs/1303.5083).
- [43] W. Fang, B. Li, and G.-B. Zhao, New probe of departures from general relativity using minkowski functionals, *Phys. Rev. Lett.* **118**, 181301 (2017), [arXiv:1704.02325 \[astro-ph.CO\]](https://arxiv.org/abs/1704.02325).
- [44] C. Parroni, V. F. Cardone, R. Maoli, and R. Scaramella, Going deep with minkowski functionals of convergence maps, *Astron. Astrophys.* **633**, A71 (2020), [arXiv:1911.06243 \[astro-ph.CO\]](https://arxiv.org/abs/1911.06243).
- [45] K. Aylor, M. Haq, L. Knox, Y. Hezaveh, and L. Perreault-Levasseur, Cleaning our own dust: Simulating and separating galactic dust foregrounds with neural networks, arXiv preprint [arXiv:1909.06467](https://arxiv.org/abs/1909.06467) (2019).
- [46] D. K. Ramanah, T. Charnock, F. Villaescusa-Navarro, and B. D. Wandelt, Super-resolution emulator of cosmological simulations using deep physical models, arXiv preprint [arXiv:2001.05519](https://arxiv.org/abs/2001.05519) (2020).
- [47] A. Tamosiunas, H. A. Winther, K. Koyama, D. J. Bacon, R. C. Nichol, and B. Mawdsley, Towards universal cosmological emulators with generative adversarial networks (2020), [arXiv:2004.10223](https://arxiv.org/abs/2004.10223).
- [48] D. Bau, J.-Y. Zhu, J. Wulff, W. Peebles, H. Strobelt, B. Zhou, and A. Torralba, Seeing what a gan cannot generate, in *Proceedings of the IEEE International Conference on Computer Vision* (2019) pp. 4502–4511.
- [49] J. Bruna, S. Mallat, E. Bacry, J.-F. Muzy, *et al.*, Intermittent process analysis with scattering moments, *The Annals of Statistics* **43**, 323 (2015).
- [50] G. Jung, B. Racine, and B. van Tent, The bispectra of galactic CMB foregrounds and their impact on primordial non-Gaussianity estimation, *Journal of Cosmology and Astroparticle Physics* **11**, 047.